Numerical Modeling of Methane Venting from Lake Sediments

by

Benjamin P. Scandella

Submitted to the Department of Civil and Environmental Engineering
in partial fulfillment of the requirements for the degree of

Master of Science in Civil and Environmental Engineering

at the

MASSACHUSETTS INSTITUTE OF TECHNOLOGY

September 2010

Author .....
Department of Civil and Environmental Engineering
August 6, 2010

Certified by .....
Ruben Juanes
Assistant Professor of Civil and Environmental Engineering
Thesis Supervisor

Accepted by .....
Daniele Veneziano
Chairman, Departmental Committee for Graduate Students

Numerical Modeling of Methane Venting from Lake Sediments

by

Benjamin P. Scandella

Submitted to the Department of Civil and Environmental Engineering
on August 6, 2010, in partial fulfillment of the
requirements for the degree of
Master of Science in Civil and Environmental Engineering

Abstract

The dynamics of methane transport in lake sediments control the release of methane into the water column above, and the portion that reaches the atmosphere may contribute significantly to the greenhouse effect. The observed dynamics are poorly understood. In particular, variations in the hydrostatic load on the sediments, from both water level and barometric pressure, appear to trigger free gas bubbling (ebullition). We develop a model of methane bubble flow through the sediments, forced by changes in hydrostatic load. The mechanistic, numerical model is tuned to and compared against ebullition data from Upper Mystic Lake, MA, and the predictions match the daily temporal character of the observed gas releases. We conclude that the combination of plastic gas cavity deformation and flow through "breathing" gas conduits explains methane venting from lake sediments. This research lays the groundwork for integrated modeling of methane transport in the sediment and water column to constrain the atmospheric flux from methane-generating lakes.

Thesis Supervisor: Ruben Juanes
Title: Assistant Professor of Civil and Environmental Engineering

Acknowledgments

I would like to thank my advisor, Ruben Juanes, for his consistent encouragement and constructive feedback during the research and writing process. This thesis would not have been possible without the data set collected by Charuleka Varadharajan and Harold Hemond (with help from the rest of the Hemond lab). Their suggestions, as well as those of labmates Luis Cueto-Felgueroso, Ran Holtzman, Chris MacMinn and Michael Szulczewski and researchers Franz-Josef Ulm, Peter Flemings, Bernard Boudreau, Dani Or, Kevin Mumford, Jiri Mikyska and Carolyn Ruppel, helped to form the model presented here. Special thanks are due to Carolyn Ruppel, who involved me in geophysical field work and contributed the seismic and sonar images presented here.

I am grateful to my fellow students, among them Shani Sharif, Peter Kang, Aldrich Castillo, Teresa Yamana, Chelsea Humbyrd, Kyle Peet, Alison Takemura, Daniel Livengood, Sidarth Rupani, Kurt Frey, and many others, for celebrating the good times and trudging through the hard with me. The Parsons Laboratory is a supportive community thanks to people like Gajan Sivandran, James Long and Sheila Frankel, and the departmental staff including Kris Kipp, Jeanette Marchocki and Patricia Glidden have helped me navigate the maze of MIT. Finally, I thank my parents, Nancy Haigwood and Andy McNiece, Carl and Carole Scandella, brothers Aiden and Nathan, grandmother Nan Haigwood, Boston family Jan and Joe Hankins, and my wonderful extended family for believing in me.

Contents

List of Figures

List of Tables

Chapter 1

Introduction

1.1 Motivation

Methane is a potent greenhouse gas, and the contribution of lakes to the present and future atmospheric methane source remains uncertain [57]. Over a century, a molecule of CH_4 captures 25 times as much radiative energy as one of CO_2. This large global warming potential causes anthropogenic methane emissions to constitute 17% of the radiative forcing from all long-lived greenhouse gases [57]. Methane emissions from lakes, however, are neglected in methane budgets and global circulation models, despite recent evidence that this source may be larger than originally estimated (See Table 1.1) [8, 12, 68]. Accurately estimating the contribution from various sources is crucial to bracketing the risks associated with climate change because these sources each respond differently to variations in climate.

Attribution of methane emissions to sources is relatively easy for anthropogenic sources but not natural ones. Emissions from industry, agriculture, and biomass burning may be estimated using bottom-up techniques to extrapolate well-understood chemical processes over well-constrained regions of application [12]. Emissions from natural sources like lakes, however, are patchy in space and episodic in time, and the dominant release mechanisms at play have not been identified [68, 66]. So, extrapolating measurements taken over short time periods or with little spatial coverage underestimate the strength of natural sources. Inverse techniques may attribute the

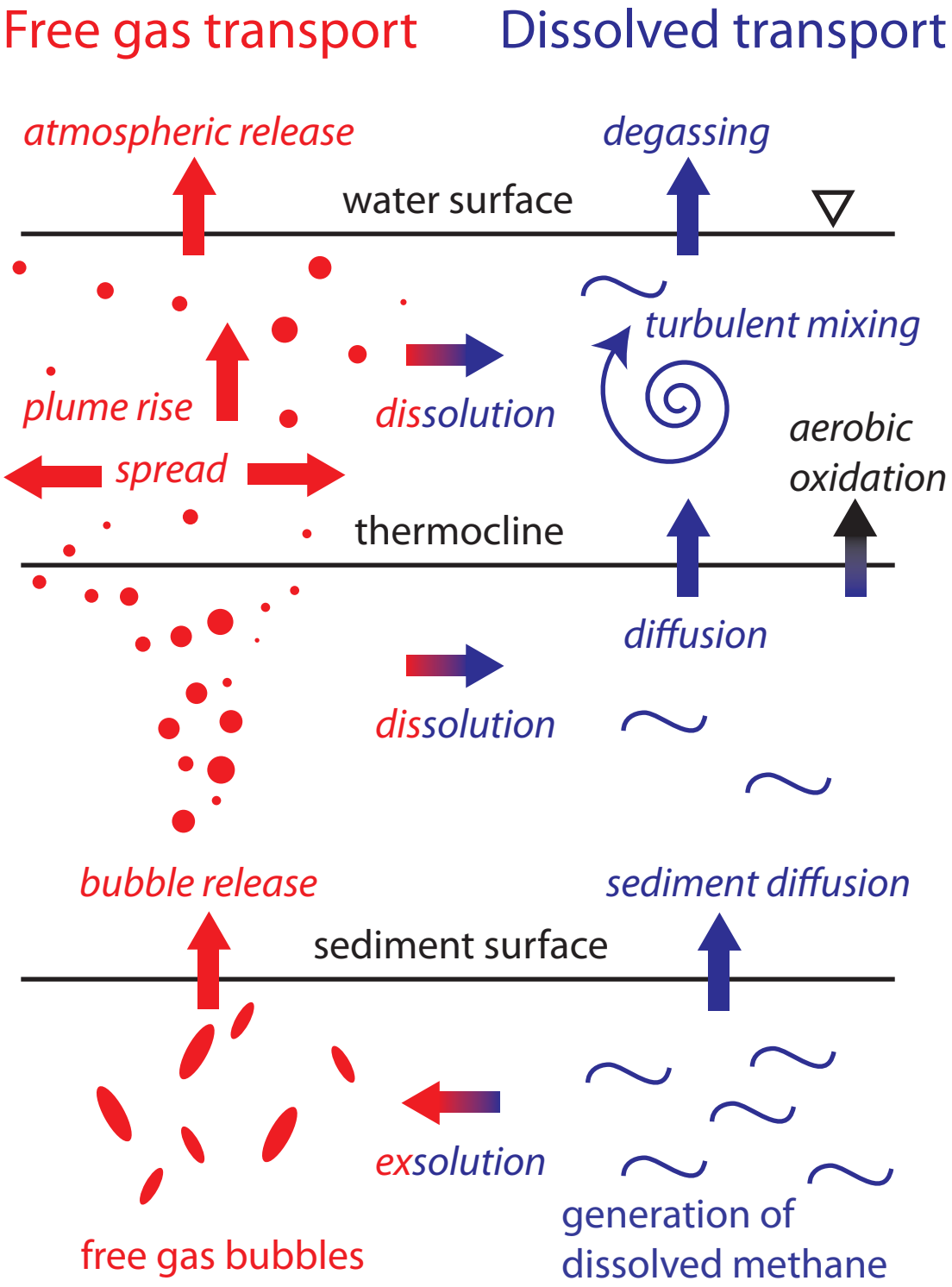

Figure 1-1: Diagram showing relevant processes for vertical methane transport related to ebullition.

observed atmospheric accumulation to a limited number of sources, but so far lakes have been lumped into the same behavior category as wetlands in such work [7, 8]. The goal of this research is to model the dominant methane release mechanism from lakes to improve future bottom-up estimates of their contribution to the global methane source. A mechanistic understanding of lake methane emissions will also indicate whether they behave differently enough from wetlands to warrant distinguishing the two sources in inverse approaches and global circulation models.

Methane is generated in anoxic sediments through microbially-mediated decomposition of organic matter [78]. It may be transported to the lake surface via two primary pathways diagrammed in Figure 1-1: dissolved advection-diffusion and free-gas bubbling, called ebullition. From its origin in the sediments, some dissolved methane diffuses into the water column, but at high concentrations it exsolves into gas bubbles that grow in and eventually escape from the sediments. These bubbles efficiently transport methane due to buoyancy and high methane content, and field studies suggest that they are the dominant mode of atmospheric release (see Table 1.2) [10, 44, 31, 49, 68, 66, 11]. Some portion of the methane dissolves from the bubbles during their rise to the lake surface, and the dissolved methane may either be oxidized to carbon dioxide or be transported to the surface by turbulent mixing. The amount lost to dissolution depends on the spatial and temporal concentration of gas release because large bubble plumes create upwelling currents and locally saturate the water with methane [38, 37, 19]. Bubble dissolution may also depend on the mode of release because smaller bubbles dissolve faster [45], and the bubble size distribution may depend on the rate of gas release [22]. A mechanistic model of methane release must then reproduce the spatiotemporal concentration of free-gas releases to correctly predict the fraction that escapes dissolution and reaches the atmosphere.

The mechanistic model presented below was inspired by two key observations. The first is a sharp rise in ebullition events during periods of falling or low hydrostatic pressure, the combination of water depth and barometric pressure that presses on the sediment surface [43, 16, 77]. In particular, a high-resolution record of surface bubble flux and hydrostatic pressure measurements on Upper Mystic Lake (UML), Mas-

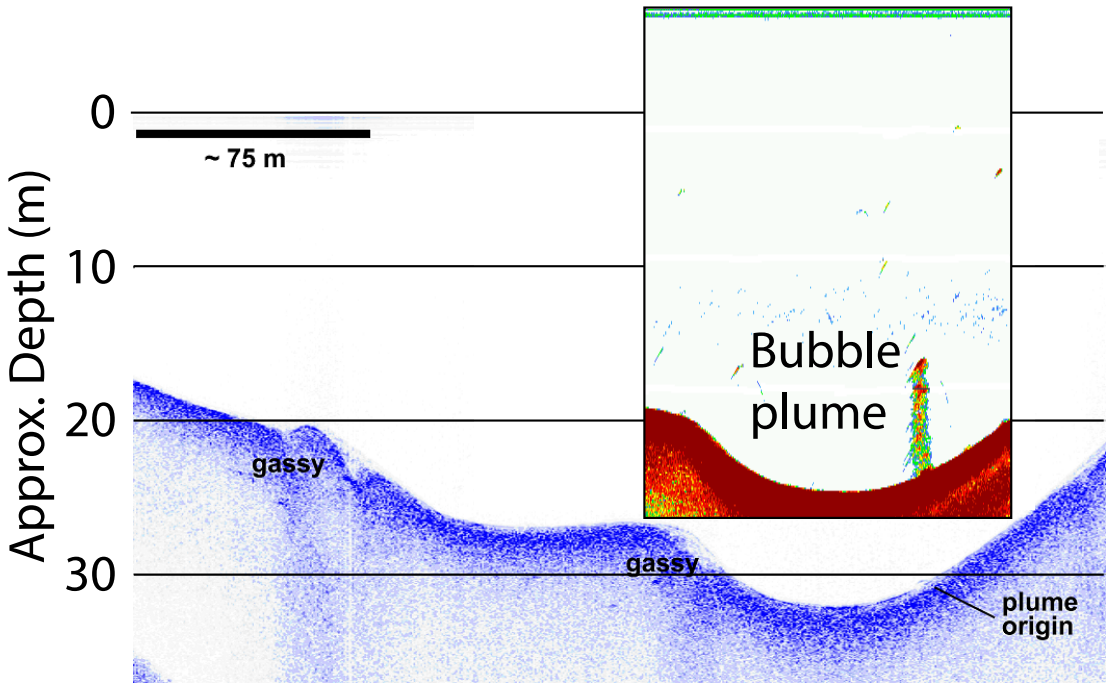

Figure 1-2: Seismic trace of the sediments in UML, showing distinct gas-bearing sediment regions. Inset: sonar trace showing a bubble plume rising from the same sediment location. Courtesy of Carolyn Ruppel, USGS.

sachusetts shows a strong nonlinear relationship between these two [66]. An acoustic image of gas-bearing sediments and a plume rising from them in UML is shown in Figure 1-2. The second key observation is the importance of grain rearrangement and the formation of fractures or conduits for gas bubble growth and transport in fine, shallow sediments [55, 4]. To incorporate both of these observations in predicting the release of methane from lake sediments, we hypothesize that gas bubbles escape by dilating conduits to the sediment surface during periods of falling hydrostatic pressure as the gas bubbles overcome the confining stress from the sediments. This model of "breathing" dynamic conduits for gas release couples continuum-scale poromechanics theory with multiphase flow in porous media to predict the temporal signature of ebullition, which impacts the fraction of methane generated that escapes to the atmosphere.

This thesis describes the development, verification and validation of this mechanistic model of methane ebullition from lakes. In Section 1.2 we review the physical

processes involved in methane generation and bubble formation, release, and rise through the water column. These processes are simplified and expressed mathematically in Chapter 2 on the model development. The model is tested in Chapter 3 for sensitivity to unconstrained parameters and then validated against a data set of ebullition measurements from UML, a typical mid-northern latitude lake in many respects, in Chapter 4. Chapter 5 discusses the results and concludes that multiphase gas flow through dynamic conduits is a valid mechanism to model the concentration of ebullition at the daily time scale and lake-wide spatial scale.

1.2 Physical processes

This section describes part of the methane cycle in lakes associated with atmospheric releases. Relevant processes are discussed below and diagramed in Figure 1-1.

1.2.1 Methane generation in lake sediments

Methane is generated in anoxic lake sediments by microbial decomposition of organic matter [29]. As formerly live matter sinks and is progressively buried, the organic carbon is respired by microbes. The most energetically-favorable electron acceptors are utilized first and highest in the sediment column until the depth where each is depleted, in the order of oxygen, manganese(IV), nitrate, iron(III), and finally sulfate [29]. At the bottom of this reduction-oxidation chain, bacteria anaerobically ferment organic carbon to make hydrogen (H_2) and acetate (CH_3COOH), which are readily converted to methane with the help of archaea in close physical proximity to the fermenters. A balanced reaction with the fermentation step included reads:

$$(CH_2O)_{106}(NH_3)_{16}(H_3PO_p) \rightarrow 53CO_2 + 53CH_4 + 16NH_3 + H_3PO_4, \qquad (1.1)$$

which yields 350 kJ mol^{-1} of free energy at standard conditions [29]. A dimictic lake like UML stratifies twice a year, and aerobic respiration quickly depletes the hypolimnion of oxygen while it is isolated from the atmosphere. Though shallower

sediments overlain by oxic water may contribute some methane, hypolimnetic sediments are the primary source in such a lake.

Methanogenesis rates vary both vertically and horizontally in lake sediments. They are highest in the top 10-20 cm of sediments and decrease with depth [35]. However, alternative oxidizing molecules may also consume methane in these shallow sediments so that the greatest dissolved accumulations occur 1-2 m below the sediment surface [42, 66]. From an aerial perspective, methanogenesis rates vary with organic matter input, sediment temperature and oxygen availability [32, 39]. For example, we would expect elevated methanogenesis near a river mouth due to the focused organic matter deposition. In addition, the close-proximity microbial consortia that link fermentation and methanogenesis occur in patches, and these patches may further concentrate generation [25]. As methane concentrations rise locally, the solute diffuses and smooths concentration gradients. However, the combined low solubility in shallow lake sediment pore water ($\sim$ 5 mM at 2.5 atm and 5° C [14]) and low intrinsic fluid flow permeability of the fine-grained sediments ($k \leq 10^{-16}$ m^2) suggests that diffusion does not act over large spatial scales.

1.2.2 Bubble exsolution

Once the total pressure of all the dissolved gases exceeds the hydrostatic pressure, the gases exsolve into a bubble. The equilibrium partial pressure of methane within a bubble may be related to the aqueous concentration using Henry's law:

$$P = k_H C, \tag{1.2}$$

which states that the pressure P is proportional to the dissolved concentration C. For an ideal gas at constant temperature, Henry's law implies that the volumetric solubility ω, the volume that the dissolved gas would occupy at local conditions, is constant. We can imagine a fixed volume fraction in the water into which gas may be compressed by increasing the free gas pressure [71]. For pressure and temperature conditions typical of lake sediments sediments (2.5 atm and 5° C), $\omega \approx 5\%$ [14],

meaning that equal amounts of gas may be stored as bubbles and solute if the volume fraction of gas in the fluid phases, or saturation, is about 5%. This dissolved store may then replenish the population of bubbles as they escape because the gas pressure drops and drives exsolution.

The character of bubble exsolution depends on whether bubbles may grow within existing pores or must force open their own cavities. Both theory and observation suggest that bubbles in lake sediments grow by cavity expansion. Because of the interfacial energy associated with a gas-water interface, bubbles are only stable with a minimum size. The Young-Laplace equation describes the equilibrium pressure difference between the gas inside and water outside of a gas bubble, or capillary pressure P_c, as the product of surface tension T and curvature κ:

$$P_c \equiv P_g - P_w = \kappa T \tag{1.3}$$

And for a spherical bubble with radius r, $\kappa = 2/r$:

$$P_c = \frac{2T}{r} \tag{1.4}$$

The excess interfacial energy imposes a minimum stable bubble size, below which the capillary and gas pressures would be too high and the bubble would dissolve or depressurize by expansion. The characteristic grain size of mud is approximately 10 μm [24] and the largest void spaces are smaller than 100 μm [55]. If a bubble was to grow in a 10 μm-sized pore, the equilibrium capillary pressure from Laplace's equation would be

$$P_c = \frac{2T}{r} \approx 30 \text{ kPa}, \tag{1.5}$$

where $T = 0.07$ N/m is the methane-water interfacial tension [54]. This capillary pressure is larger than the contact pressure between grains in the first few meters of sediment

$$\sigma'_{vw} \approx (\rho_b - \rho_w) g d < 5 \text{ kPa}, \tag{1.6}$$

where ρ_b and ρ_w are the bulk and water densities, g the gravitational constant, and

d the depth within the sediments. So, a micron-sized bubble could not be stably trapped in shallow sediments.

Observations of gas bubbles grown in shallow marine sediments confirm that the minimum size of bubbles is much larger than the characteristic grain size [27] and that addition of gas to synthetic mud samples creates pores in the 200-500 μm range that did not exist in water-saturated samples [48, 61, 55]. Based on visual observations of the fine sediments below UML, we expect the same conditions in lakes. Apparently, gas bubbles cannot fit within the existing pores and must rearrange solid grains to open their own pore cavities. These large, highly-compressible inclusions within a water-saturated sediment matrix should have markedly different behavior than saturated soil containing interstitial bubbles.

The relative sizes of grains and bubbles impacts the pressure and volume changes of exsolving bubbles. If the bubbles were smaller than the grains and able to grow by squeezing through pore throats without moving grains, we would expect gas bubbles to grow first in the largest pores. With rising gas pressure, they would either nucleate in smaller pores or invade through similarly-sized throats between sediment grains. Grain-scale numerical simulations demonstrate how this capillary invasion mode only occurs for relatively large grains, and that gas invades fine-grained sediments, like lake mud, by fracturing [26]. Experiments on gas bubble growth in marine mud confirm that the bubble pressure rises until the it is sufficient to force grains apart, expand the bubble and reduce the gas pressure [27]. X-ray CT scans of this same process show that bubbles grow as sub-vertical, cornflake-shape fractures [4]. The cycle of pressurization and expansion repeats and forms a saw-toothed pressure history with no long-term trend of rising pressure.

While experiments show that the gas pressure in a bubble varies as it grows, the magnitude of the variation may be small relative to the hydrostatic forcing. The height of the pressure "teeth" is less than 5 kPa, and smaller for less-cohesive sediments that allow the bubble to expand more as if in a fluid rather than a solid [27]. Visual inspection of samples of UML sediments suggest that the top few decimeters are very poorly cohesive, which would suggest minimal bubble pressurization. In

addition, bubble pressurization in the Johnson *et al.* (2002) experiments may be exaggerated, compared with natural settings, because they injected gas through a fine needle rather than allowing bubbles to exsolve from supersaturated water on all sides [27]. Therefore, the pressure and volume evolution during exsolution should reflect something between discrete fracture events and continuous expansion in fluidized sediments.

A final forcing on the partitioning of methane between the aqueous and gaseous phases is temperature. The Henry's law constant k_H increases with temperature, or equivalently the volumetric solubility ω decreases. Then rising temperatures spur exsolution and have been implicated in initiating ebullition events in shallow estuaries and lakes [6, 11]. In UML, however, the thermal stratification ensures that the temperature over the hypolimnetic sediments stays between 4 and 6° C [66]. So, the impact of temperature variations on ebullition should be small, except when seasonal temperature changes destroy the stratification and cause lake-wide mixing.

Exsolution of dissolved methane into free gas bubbles appears to be one controlling factor on the rate of methane release to the atmosphere. The complex mechanisms presented here will be parameterized in Chapter 2 as part of predicting the rate of ebullition. The fate of exsolved bubbles depends on their evolution and transport, subjects treated in the next sections.

1.2.3 Bubble evolution with hydrostatic pressure variations

Bubble exsolution may be fairly insensitive to temperature changes in stratified lakes, but hydrostatic pressure fluctuations impact the gas pressure and volume and thereby the conditions for gas release from sediments. This hydrostatic forcing, the sum of contributions from water level and atmospheric pressure, pushes on the top of the sediment column and compresses the individual components to different degrees. This section will introduce relevant poromechanics concepts, including effective stress, and review two experiments that shed light on the nature of the response in gassy sediments.

When a sample of solid material is subjected to a stress, or force per area, it

responds by deforming its shape. The nature of this strain, or relative displacement, depends on whether the work applied is stored as potential energy or released as heat or entropy generation. Elastic deformations store all the work in reversible strain and rebound to their rest configuration when the applied stress is removed. Linear elastic strain $\boldsymbol{\varepsilon}$ is proportional to the applied stress $\boldsymbol{\sigma}$:

$$\boldsymbol{\sigma} = \mathbf{C} : \boldsymbol{\varepsilon} \tag{1.7}$$

where the bold indicates the tensorial nature of stress and strain and $\mathbf{c}$ is stiffness tensor [9]. Purely plastic deformations, on the other hand, dissipate the energy during irreversible deformation and maintain their final configuration when released. Both types of deformation may occur within gassy sediments simultaneously, but we attempt to identify conditions when one or the other dominates.

In a porous medium, the response of the solid and fluid components depends on their compressibilities and the nature of the fluid flow. The hydrostatic load imposes a stress on the sediments that is born to different extents by the solid and fluid phases. Compression of the solid skeleton adds to the fluid pressure and drives fluid flow. If the rate of loading is slow relative to the solid permeability to flow, then any excess pore pressure is diffused away until the profile becomes hydrostatic within the porous medium. This is known as a drained response. For low-permeability sediments, however, rapid changes in hydrostatic loading can cause significant fluid pressures in excess of their hydrostatic profiles. The limiting response with negligible fluid outflow and pressure diffusion is called undrained [69]. Distinguishing between drained and undrained responses is useful for modeling gassy sediments and will be addressed below.

We can identify the elastic-plastic nature of gassy sediments using a published experiment on compression of sythetic samples. Thomas (1987) progressively loaded a sample of synthetic sediments saturated with water and gas bubbles with a unaxial stress from 0 to $\sim$ 400 kPa and then slowly removed it, all the while recording the change in total volume (strain) and fluid volume released [61, 55]. The difference

he attributed to change in gas volume, and by assuming the gas was ideal and that dissolution followed Henry's law, he calculated variations in the gas pressure. The initial value of gas pressure was assumed equal to the total vertical stress, though it could have been lower than this. Even though the drained experiment setup permitted the water pressure to dissipate during loading, the gas bubbles remained trapped in relatively large cavities that shrunk and pressurized. The gas pressure rose during the loading phase but did not begin to fall during unloading until after the imposed stress dropped below the gas pressure (see Figure 2-2A). If the bulk response had been purely elastic, the sample would have stored the energy associated with compressing it and released that energy by decompressing the gas as soon as the load was reduced. The fact that it did not implies that the gas was pressurized by an irreversible rearrangement of the grains to reduce the cavity volume. Based on these observations and scanning electron microscope images of the synthesized gassy sediments, the authors propose a conceptual model where large, gas-filled cavities expand and contract within continuous, plastically-incompressible matrix of sediment and water. These experiments may not be directly applicable to lake sediments, which are subject to smaller variations in hydrostatic load ($\sim$ 5 kPa), are less consolidated in the top few decimeters, and may have lower gas content. Still, they indicate that plastic cavity contraction and expansion may play a central role in the pressure-stress evolution.

In understanding the plastic and elastic responses of porous media, effective stress is a useful concept. Effective stress may be generally defined as the force normal to a cross-sectional area that is transmitted through particles within that area, divided by the area [51]. This stress transmitted through particles is reduced by interstitial fluid pressure, which effectively cushions the grains. Because it depends on both bulk stress and pore fluid pressure, effective stress is used in our model to constrain the evolution of gas bubble pressure as the hydrostatic load rises and falls. In poromechanics theory, effective stress simplifies analysis, for example by permitting a linear relationship between effective stress and strain [9]:

$$\boldsymbol{\sigma}' = \mathbf{C} : \boldsymbol{\varepsilon}, \tag{1.8}$$

where $\boldsymbol{\sigma}$ is the total stress tensor, $\boldsymbol{\varepsilon}$ is the strain tensor, and $\mathbf{C}$ is a fourth-order stiffness tensor. Terzaghi (1925) performed experiments on porous media filled with a single fluid phase and suggested that the effective stress

$$\boldsymbol{\sigma}' = \boldsymbol{\sigma} - P_f \mathbf{I} \tag{1.9}$$

was the primary determinant of soil behavior [60]. Various modifications to this expression have been suggested. To account for the compressibility of the solid grains, Biot (1941) proposed:

$$\boldsymbol{\sigma}' = \boldsymbol{\sigma} - bP_f \mathbf{I}, \tag{1.10}$$

where b is Biot coefficient, which reduces to 1 for incompressible solid grains [1, 69, 9]. For sediments with gas and water, Bishop (1959) included χ, the fraction of solid surface contacting the water [2, 72]:

$$\boldsymbol{\sigma}' = \boldsymbol{\sigma} - [P_g + \chi(P_g - P_w)]\mathbf{I} \tag{1.11}$$

Others have proposed more complex variations in order to define a thermodynamically-consistent quantity [20]. However, the desire for simplicity in the mechanistic model developed here motivates an especially simple expression.

Another experiment performed by Thomas (1987) helps to identify the applicable effective stress in gassy sediments. The sediment sample was compressed over a week while the water drainage ports were alternately opened and closed to capture both drained and undrained fluid responses. The volume and stress changes throughou were tracked throughout the experiment, and the results showed that there was no unique relationship between the total porosity changes or total strain and the vertical consolidation stress, σ'_{vw}:

$$\sigma'_{vw} = \sigma_v - P_w \tag{1.12}$$

where the v subscript indicates that the stress is in the vertical direction only and w that it considers only water pressure. Terzaghi would have predicted a linear relationship between this effective stress and total strain for water-saturated soils,

and this experiment shows how gassy soils behave differently [60]. The experiment at hand did yield a unique relationship, however, between σ'_{vw} and the volume fraction, of the combined water and solid phases, occupied by water. Because both of these constituents are relatively incompressible, the porosity of the grain-water matrix only changed during the drained phases of the experiment due to water loss, and the vertical consolidation stress captured this mud water porosity loss [61]. If we were interested primarily in capturing the flow of water in lake sediments, then the vertical consolidation stress would be the best choice for an effective stress to consider.

However, we are interested in the gas pressure evolution. Thomas' experiment showed that there was a strong relationship between the total vertical stress and the gas volume and pressure. Considering that the sediment and water are both less compressible than the gas voids, it becomes appealing to consider the three-phase porous medium from a different perspective. Instead, we may model the system as gas voids surrounded by a combined water-grain phase that as a whole acts the role of the solid in two-phase poromechanics [76, 55]. In this case, the porosity of interest is the gas volume fraction, changes in which equal the bulk volumetric strain. Our interests shift from considering the inter-granuar stresses in water-saturated porous media to the bulk stress holding the grain-water matrix against displacement by large gas voids in lake sediments. So, we propose that the appropriate effective stress does not contain the pressure of water, but of gas:

$$\sigma'_{hg} = \sigma_h - P_g. \tag{1.13}$$

This gas horizontal effective stress may be used to quantify changes in gas pressure and volume and to predict the transition between elastic and plastic behavior. This model will be developed in Chapter 2.

1.2.4 Ebullition

While understanding of the impact of hydrostatic pressure fluctuations on trapped gas bubbles is mostly based on poromechanics theory, its impact on ebullition is a

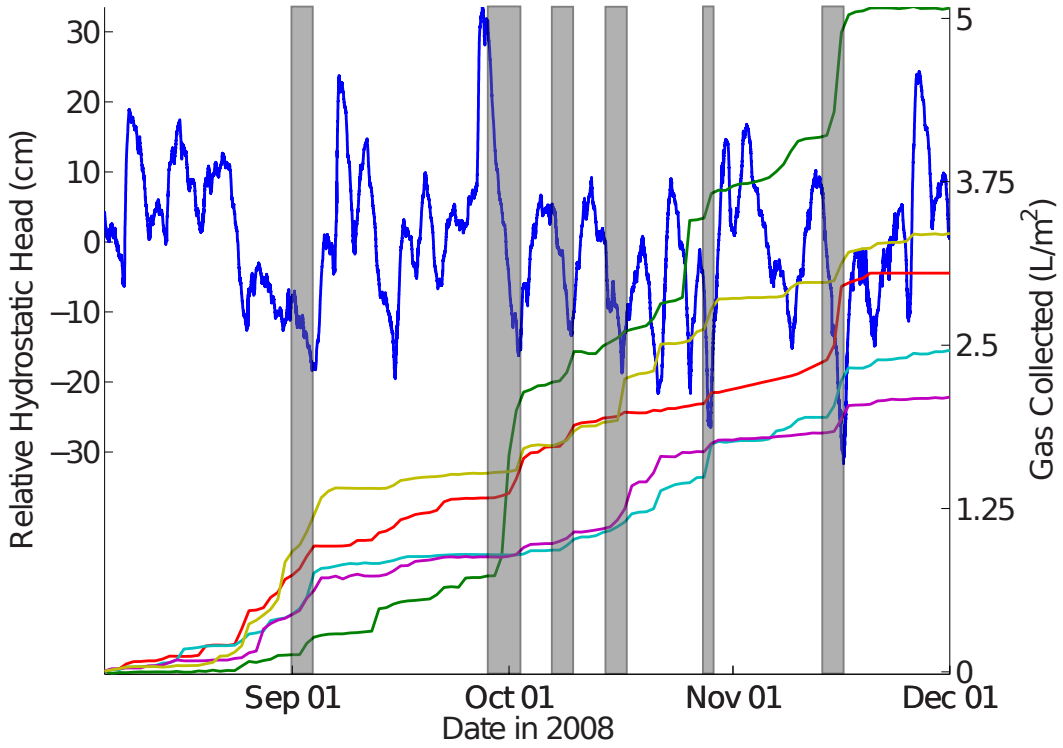

Figure 1-3: Record of hydrostatic head variations (left axis, blue) and cumulative gas collected (right axis) from five traps moored just below the surface of UML. The flux records from individual traps show some synchronicity especially during periods of pronounced drop in hydrostatic head (gray bars)

process well-observed but as of yet not mechanistically modeled. This section reviews observations of methane ebullition from lakes and highlights a record of ebullition and hydrostatic pressure variations that is used to validate the proposed model.

We can gain some insight into the character and mechanism of ebullative methane venting from observations of bubble growth and release into overlying water. In some settings temperature changes [11] and wind-driven shear [28] seem to trigger release events, but perhaps the best-established forcing for ebullition is hydrostatic pressure variation. Studies have documented tidal influence on bubbling from estuarine [43] and ocean [63] sediments, as well as the influence of water level change on peatland ebullition [16, 62]. Contributing to observations of the relationship between ebullition and hydrostatic pressure on lake sediments [59, 44, 68, 11], or its rate of change [77], is a data set recently recorded in Upper Mystic Lake (UML), a temperate, eutrophic

Figure 1-4: Image of a bubble trap on a dock at UML. The funnel at bottom collects gas bubbles into the PVC cylinder, and the buoyancy of the gas column allows the pressure sensor at top to estimate the collected volume. The traps were suspended about 1 m below the water surface by the buoy. Courtesy of Charuleka Varadharajan.

lake north of Boston, MA (see Figure 1-3). Wavelet analysis of the gas flux record shows significant variability in the timing, magnitude and locality of ebullition events and a nonlinear relationship with hydrostatic pressure.

The data were collected using surface-buoyed bubble traps – inverted funnels connected to PVC pipes that collect a column of free gas (Figure 1-4. A pressure sensor measures the buoyant force from the gas as a proxy for the column height, which allows estimation of the rate at which gas enters the funnel [66]. While the data were recorded at five-minute resolution, surface waves corrupted the high-frequency signal with pressure artifacts that imply negative bubble fluxes to the atmosphere (Figure 4-2). These artifacts are partially removed by applying a one hour moving-average filter to the flux data and then binning it into either hourly or daily flux values. The hydrostatic pressure data are also smoothed using the moving-average filter and passed to the model as a cubic spline with hourly resolution.

While there appears to be a relationship between ebullition and hydrostatic pressure, or its rate of change, the data from [66] show that neither relationship is linear. Figure 1-5 shows that the daily gas volume flux is poorly correlated with both the

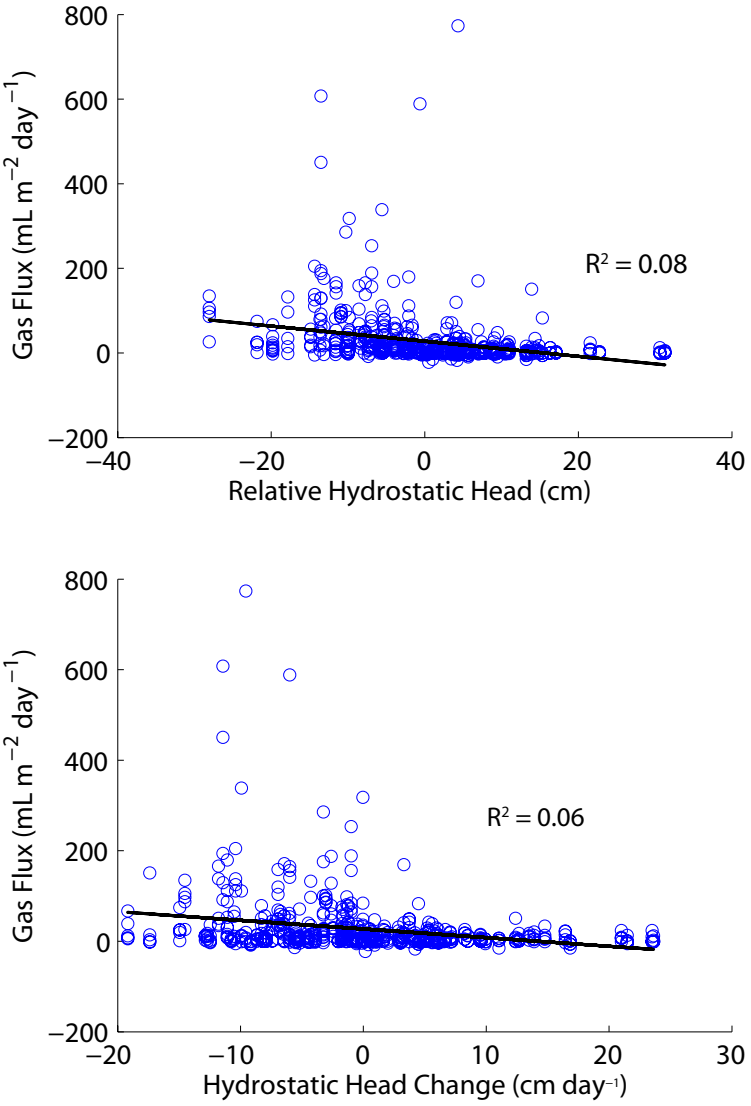

Figure 1-5: Correlations between daily volumetric gas fluxes and (top) relative hydrostatic head and (bottom) daily shift in relative hydrostatic head.

relative hydrostatic head (around its seasonal mean) ($R^2 = 0.08$) and the daily shift in hydrostatic pressure ($R^2 = 0.06$). The correlation coefficients are even smaller for hourly fluxes and hydrostatic pressure ($R^2 = 0.02$) and pressure shift (0.01). A valid model of ebullition must then capture the nonlinear relationship between gas flux and compression of the sediments.

Gas bubbles are buoyant with respect to water and sediment grains, and falling hydrostatic load on the sediments clearly provides a mechanism for gas to deform the sediments. However, theoretical analysis shows that spherical bubbles of realistic size require storm-surge vertical stress variations, on the order 7.5 m of water head, to be mobilized for vertical flow in sediments with reasonable shear strength [75]. This implies that some other mechanism must mobilize bubbles for vertical transport. The fact that bubbles grow in a cornflake-shaped fracture pattern [4], rather than as spherical bubbles, suggests that this mode of growth may also allow for vertical mobility. Fracturing has been implicated as a dominant mechanism for vertical gas transport in methane hydrate-bearing ocean sediments [17, 41]. Following these observations, we hypothesize that the dilation of sub-vertical conduits for free-gas flow is exactly this missing mechanism.

1.2.5 Rise through the water column

Bubbles released from gassy sediments shed methane as they rise through the water column, and the amount lost to dissolution depends on the partial pressures of methane in the gas bubble and surrounding water, as well as the time the bubble spends in transit. These in turn depend critically on the initial size and release depth (Figure 1-6), as well as the spatial and temporal concentration of gas release. Large bubble plumes create upwelling currents and locally saturate the water with methane, inhibiting dissolution and keeping methane in rising bubbles inaccessible to oxidizing microbes [38, 37, 19]. The mechanism and rate of methane ebullition clearly impact the plume effects, but they may also influence the bubble size distribution [22, 64]. A mechanistic model of methane release must then reproduce the spatiotemporal concentration of free-gas releases to correctly predict the fraction that escapes dissolution

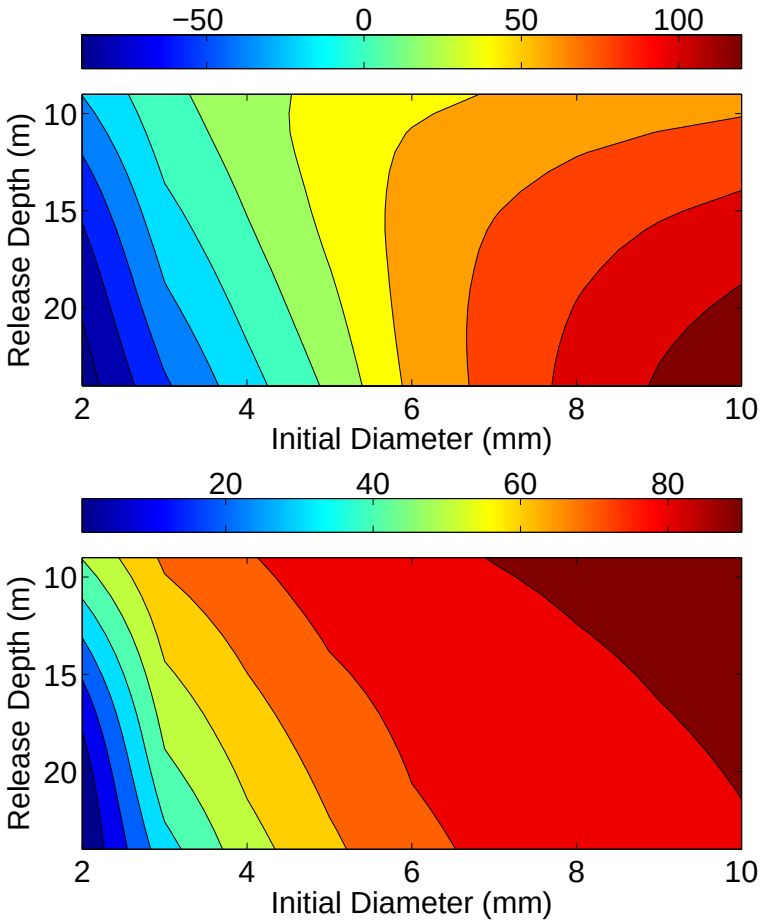

Figure 1-6: Impact of dissolution and depressurization on a rising bubble: (top) percent change in bubble volume and (bottom) CH_4 mass percent at the surface for pure methane bubbles of various initial sizes released from multiple depths in the range of conditions for hypolimnetic sediments in UML. Water data from [66] were used as inputs for the Single Bubble GUI model [21].

and oxidation and enters the atmosphere.

An order of magnitude estimate suggests that plume effects should be minimal in Upper Mystic Lake. The record of ebullative fluxes presented by Varahdarajan (2009) included peak releases of up to 60 L m^2 $day^{-}1$ [66]. If we assume a constant rise of 6 mm diameter spherical bubbles at 25 cm s^{-1} [45], then the bubble density just below the surface would be about 20 m^{-3}. This would not be sufficient to call the bubbles a plume, however the density may be higher in plumes at the sediment surface or in ebullition events not captured by the eight bubble traps deployed without knowledge of bubbling sites.

Methane dissolved in the water column is vulnerable to oxidation by chemosynthetic microbes [29]. In oxic waters, the reaction:

$$CH_4 + 2O_2 \rightarrow CO_2 + 2H_2O \qquad \Delta G_0 = -810 \text{ kJ mol}^{-1}, \tag{1.14}$$

transforms methane into the less-potent greenhouse gas, CO_2. During the summer and fall, the hypolimnion is depleted of its oxygen by respiration and is not replenished by mixing due to the stable density stratification. Significant quantities of methane may be stored in the anoxic hypolimnion [66], and aerobic oxidation occurs primarily at the thermocline, where oxygen diffuses down from the epilimnion (Figure 1-1).

This storage condition breaks down with late fall surface cooling that erodes the stratification and mixes the lake [29]. During mixing, some portion of the dissolved methane is oxidized by the newly-infused oxygen, while the rest degasses to the atmosphere if it is advected to the surface. One study found that only 7% of the dissolved methane was oxidized at the thermocline during summer stratification, but 60% was oxidized during fall overturn and 40% escaped to the atmosphere [52, 59]. Further study of methane during turnover is required to improve estimates of the mass released to the atmosphere and to quantify the impact of bubble dissolution that may depend on the mode of release.

1.3 Previous integrated modeling

Mechanistic modeling of methane-venting sediments remains in its infancy. Some speculate that releases from the oceanic sediments occur by activation of successively smaller pore throats with rising capillary pressure during periods of falling hydrostatic pressure [3, 36]. Arguments based on analysis of the Fourier spectrum and phase lag of venting events with surface waves suggest that pore throat activation may be dominant in coarse marine sediments, but likely not so in fine lake sediments. Some mechanistic numerical modeling was performed by [46], who treated methane release from marine sediments as multiphase flow through porous media. However, their steady-state model predicted no gas release at the sediment surface so cannot explain the dynamic release structure observed at UML. A mechanistic model of multiphase flow in static vertical sediment conduits was used to explain deep pore water irrigation observed near oceanic vent sites [23]. However, no ebullition data was available for comparison. We seek to validate the mechanism of flow through *dynamic* sediment conduits by comparing predictions of fluxes from a model venting site, forced by observed hydrostatic load variations, against field recordings of those ebullative fluxes. This work can both expand our understanding of coupled flow and mechanics problems in poorly-cohesive sediments and lay the groundwork for predicting the upscaled atmospheric methane release from lakes.

Table 1.1: Estimates of global methane emissions in Tg CH_4 per year. Figures from [68] suggest a $10 - 60\%$ increase over previous estimates of methane emissions from Northern lakes and wetlands combined, yet the contribution from lakes is not included in any of [8, 57, 12]

Total Release	Wetlands	Lakes	Estimation method	Year	Source
545-1035	130-620	1.25-25	Bottom-up	1974	[15]
-	$6 - 40^{\dagger}$	$3.8^{\ddagger}$	Extrapolation	2006	[68]
596-597	120-180	-	Inverse	2006	[8]
582	100-231	-	All	2007	[57, 12]

†: Northern wetlands only. ‡: North Siberian lakes only

Table 1.2: Percent of atmospheric methane releases via ebullition from lakes

Percent ebullition	Water body	Year	Source
20-52	Beaver pond in Manitoba, Canada	1999	[13]
30-50	Wintergreen Lake, Michigan	1978	[59]
50	Mirror Lake, New Hampshire	1990	[44]
65	Lake Wohlen, Switzerland	2010	[11]
70	Lake Calado, Brazil	1988	[10]
70	Upper Mystic Lake, Massachusetts	2009	[66]
90	Lake Kasumigaura, Japan	1999	[49]
95	Two North Siberian lakes	2006	[68]
98	Gatun Lake, Panama	1994	[31]

Chapter 2

Model development

In the following chapter we describe how gas bubbles grow and escape from a characteristic, one-dimensional model gas venting site. The pressures and volumes of gas, water and soil are mechanistically evolved at the continuum scale for each depth in the model sediment domain in response to a fluctuating hydrostatic load on the sediment surface. Under appropriate conditions, the model predicts activation of conduits, and equations for multiphase fluid flow through the conduits yield a gas flux from the sediment column. We then place these characteristic venting sites in the context of a physical lake to compare model gas flux predictions with measurements made by randomly-placed bubble traps at the lake surface.

2.1 Model domain

The core of our model is a column of sediments with vertical extent h and lateral area A^{vent}. This column is assumed to be laterally uniform so that only vertical variations in properties need to be considered. The column is sliced into nz representative elementary volumes (REV)s, each of which is associated with a characteristic pressure and volume of the pure methane gas, pure water and solid grain phases. These state variables vary as the top boundary is forced with hydrostatic stress variations that are input using data from [66]. The fluid phases may flux across the horizontal interfaces between the REVs and, critically, out through the top boundary into the

water column. As described below, the model tracks variations in gas volume fraction, or saturation S_g, but changes in the porosity and volumetric strain in each element are neglected. Volume evolutions are forced to conserve mass, but the mass of methane is not explicitly tracked because the data used to validate the model are volumetric gas fluxes. The first step in modeling the release of methane from lake sediments is parameterizing its generation.

2.2 Gas volume generation

As mentioned in Chapter 1, gas bubbles in fine sediments expand by displacing neighboring grains, by fracturing. The pressure history of an individual growing bubble displays a cyclic, saw-toothed pattern [27]. However, our model homogenizes this process to the continuum scale by neglecting bubble pressurization with generation. Instead, gas exsolution forces constant bubble volume generation throughout the depth of our 1D model. The rate of gas volume exsolved per volume of water is labeled G_g and is the rate at which gas saturation S_g is generated. At each depth the model tracks not only the volume of gas stored, but also a characteristic gas pressure for the bubbles of interest. In essence, our model considers the rate of generation of bubbles of a characteristic size that is sufficient to transport significant methane and to reduce the curvature decrease with growth enough to define a characteristic capillary pressure (and thus gas pressure) at each depth. Smaller, higher pressure bubbles are neglected until they reach this critical size, and G_g could equally be considered a rate of transfer from the pool of small bubbles to large as a rate of exsolution.

2.3 Pressure-stress evolution

Given that ebullition appears to be controlled in lake settings by variations in hydrostatic pressure, modeling the pressure and volume responses of the gassy soil components is critical. The predicted pressure changes should determine when the gas cavities expand and contractwhile conserving the mass of gas exsolved in order

to predict the flux to the water column accurately. This section will develop the mathematical expressions for these mechanisms in the context poromechanics theory.

We begin with the derivation of state equations for an elastic-plastic porous medium, following [9] but adapted for a convention of positive compressive stress, which is more common in fluid flow modeling than solid mechanics. Consider a porous, deformable solid with a stress tensor $\boldsymbol{\sigma}$ and with porosity ϕ filled with pore fluid at pressure P_f. Assume that this porous medium is capable of plastic and elastic deformation. Then the energy dissipated by performing plastic work δW^p on the sediment is

$$\delta W^p = -\boldsymbol{\sigma} : d\boldsymbol{\varepsilon} + P_f d\phi - d\Psi_s \geq 0, \tag{2.1}$$

where Ψ_s is the free energy associated with the solid phase [9]. During elastic deformation, $\delta W^p = 0$, and we recover the elastic state equations:

$$-\boldsymbol{\sigma} = \frac{\partial \Psi_s}{\partial \boldsymbol{\varepsilon}}; \qquad P_f = \frac{\partial \Psi_s}{\partial \phi} \tag{2.2}$$

To account for plastic deformation, we split the strain and porosity:

$$\boldsymbol{\varepsilon} = \boldsymbol{\varepsilon}^{el} + \boldsymbol{\varepsilon}^{p}; \qquad \phi = \phi^{el} + \phi^{p} \tag{2.3}$$

where superscripts el and p denote elastic components of each. If we assume that the free energy in the solid phase is only due to the elastic strain and porosity changes, then it takes the form

$$\Psi_s = \Psi_s(\boldsymbol{\varepsilon} - \boldsymbol{\varepsilon}^p, \phi - \phi^p) \tag{2.4}$$

Then plugging this functional form in 2.4 and the elastic state equations 2.2 into 2.1, we find a more specific expression for the plastic work or dissipation:

$$\delta W^p = -\boldsymbol{\sigma} : d\boldsymbol{\varepsilon}^p + P_f d\phi^p \geq 0, \tag{2.5}$$

Equations 2.2 and 2.5 show that $-\boldsymbol{\sigma}$ and P_f are the thermodynamic driving forces behind the strain and porosity change in both plastic elastic regimes. Choosing

a scalar stress and strain simplifies the model considerably. The deformations we model in lake sediments are forced by perturbations in the *vertical* stress, implying that $\sigma_v = \sigma_{33}$ could be the primary stress of interest in modeling gassy sediments. However, bubbles expand in fine-grained sediments into oblate ellipsoidal,"cornflake-shaped" fractures, often in a sub-vertical orientation [4]. A fracture opens against the direction of least principal stress and extends normal to it. So, the stress that a near-vertical, oblate ellipsoidal bubble must overcome to dilate is not the vertical stress but the horizontal one, $\sigma_h = \sigma_{11}$. Along with the horizontal stress, we consider the volumetric strain, ϵ. In many materials the solid phase is plastically incompressible, meaning that the grains may move but not change volume. For example, in normally-consolidated clays, the ratio of grain to bulk compressibilities is $3 * 10^{-5}$ [56]. Where this is true, all of the plastic volumetric strain ϵ^p is due to plastic porosity change[1]:

$$\epsilon^p = \phi^p. \tag{2.6}$$

Then, equation 2.6 simplifies equation 2.5 to:

$$\delta W^p = -(\sigma_h - P_f) d\phi^p \geq 0, \tag{2.7}$$

In this case it becomes clear that the thermodynamic driving force between plastic strain and porosity change is simply the horizontal effective stress,

$$\sigma'_{hf} \equiv \sigma_h - P_f, \tag{2.8}$$

where the f subscript refers to a single fluid phase. This expression is clear for water-saturated soils, but for sediments with both continuous water phase and discrete gas bubbles, the appropriate fluid pressure must be specified.

In water-saturated rock and soil, the relationship between horizontal and vertical

[1]We only model the gas volume fraction change and neglect total deformation because, for values of $\phi_g < 0.1$, any gas volume growth $d\phi_g$ gives an order of magnitude larger percent change in ϕ_g than in the total volume.

effective stresses is often parameterized as,

$$k_0 = \frac{\sigma'_{hw}}{\sigma'_{vw}}, \tag{2.9}$$

where $k_0 \in [0, 1]$ is known as the lateral stress coefficient, and ν is the Poisson's ratio [69]. For many saturated soils, k_0 usually ranges from 0.5 to 1, and experiments suggest that equation 2.9 holds even for gassy soils and constrain k_0 to the range of 0.74-0.76 for a wide range of conditions [61]. From this we adopt $k_0 = 0.75$ for our system, acknowledging that this value may not necessarily be the most appropriate for gassy lake sediments. Estimating the horizontal stress from the vertical stress requires both the lateral stress coefficient and water pressure:

$$\sigma_h = \sigma'_{hw} + P_w = k_0\sigma_v + (1 - k_0)P_w \tag{2.10}$$

Using this thermodynamics framework, we model the response of lake sediment pressures and stresses to vertical stress perturbations from changing water level and barometric pressure.

2.3.1 Loading function

Modeling elastic-plastic deformation of gassy soils requires two elements: a loading function that defines the transition between elastic and plastic regimes, and a flow rule that defines how the plastic deformation occurs. In porous media a loading function is often assumed to have the form,

$$f(\boldsymbol{\sigma}, P_f) \geq 0, \tag{2.11}$$

where f defines the subspace of values $\boldsymbol{\sigma}$ and P_f may take[2]. When $f > 0$, the material is assumed to behave elastically, and when $f = 0$ the plastic flow rule is applied so that $(\boldsymbol{\sigma}, P_f)$ remain within the feasible region [9].

[2]Here compressive stresses correspond to positive values of $\boldsymbol{\sigma}$, however the formulation is equally valid with the opposite convention as long as the feasible region is instead defined by $f \leq 0$.

The loading function's dependence on $\boldsymbol{\sigma}$ and P_f may be simplified to a dependence on the effective stress, $\sigma'(\boldsymbol{\sigma}, P_f)$, and shear stress, $\tau(\boldsymbol{\sigma})$. Because the effective stress relates to the intergranular contact forces, the excess or loss of which being a trigger for fracture or plastic deformation, it seems a natural choice for a state variable. The Mohr-Coulomb and Drucker-Prager yield envelopes are two examples of loading functions that may be applied to porous materials using σ' and τ [9].

If gas in sediments remains in the form of interstitial bubbles without interacting directly with the solid grains, then the form of effective stress in gassy sediments would be the same as in saturated soil [58, 74]. Experiments indicate, however, that gas pressure is the primary determinant of porosity changes and volumetric strain and relates to the stress (both vertical and horizontal) [61]. Applying this observation to the model of mud as the solid phase and gas as the fluid phase, we consider the horizontal normal stress σ_h, and the gas pressure P_g as the only essential state variables for the loading function. When gas is the only fluid and the solid phase is plastically incompressible, equation 2.7 suggests that these state variables do not act independently to force deformation but through the horizontal gas effective stress, σ'_{hg}:

$$\sigma'_{hg} \equiv \sigma_h - P_g \tag{2.12}$$

If we assume that dominant shear effects are accounted for by this effective stress, then an appropriate simplified loading function is:

$$f(\sigma'_{hg}) = \frac{I + C}{2} - \left| \sigma'_{hg} + \frac{I - C}{2} \right| \geq 0, \tag{2.13}$$

where I and $-C$ denote the maximum and minimum values of σ'_{hg}:

$$-C \leq \sigma'_{hg} \leq I \tag{2.14}$$

When the material is compressed until it reaches the limit of its elastic integrity, $\sigma'_{hg} = I$, it deforms plastically by compressing the gas cavities. In the limit of unloading horizontal gas effective stress falls to an assumed cohesive strength, $\sigma'_{hg} = -C$, and

the cavities expand. For non-cohesive sediments, $C = 0$ and plastic expansion begins as soon as the gas pressure exceeds the horizontal stress.

Previous theoretical work has suggested physical estimates and scalings for C and I, the bounds on horizontal gas effective stress. Wheeler (1986) and Thomas (1987) considered a simple geometry of a hollow sphere of a rigid, perfectly plastic material. In this case, the difference in pressures outside the sphere (applied stress) and in the hollow cavity (gas pressure) is limited by a function of the shear strength s_u [72]:

$$|P_o - P_i| \leq 4 s_u \ln\left(\frac{R_o}{R_c}\right), \tag{2.15}$$

where R_o and R_c are the radius of the sphere exterior and inner cavity, respectively. The shear strength of a porous medium is the maximum amount of shear stress that can be applied to it before plastic yielding. This model suggests that, during loading with continual cavity contraction, the horizontal stress rises faster than the gas pressure as R_c shrinks and I rises. The results show exactly this qualitative effect [61]. If this isotropic model is compared with the form of our loading function in equation 2.13, it implies that $I = C$, a symmetry between the processes of plastic compression and expansion.

Following the work of Vesic (1972), they found another expression for the difference between the uniform isotropic pressure imposed on the outside of the medium and the pressure from the spherical cavity within:

$$|P_o - P_i| \leq \frac{4}{3} s_u \left(\ln\left(\frac{G_u}{s_u}\right) + 1\right), \tag{2.16}$$

where G_u is the shear modulus of the solid medium [76]. This model assumes that the saturated soil is frictionless and contains a spherical zone around the cavity in the state of plastic equilibrium, outside of which the mass remains in elastic equilibrium. This model suggests a different set of gas effective stress limits, $I = C$, that do not depend on the gas volume fraction so should remain constant unless the shear strength changes, as in a hardening process [9].

In addition to plastic deformation, a mechanism for imposing bounds on the gas

pressure in large cavities is capillary invasion and drainage [73]. They Young-Laplace equation describes how the capillary pressure, or difference between gas and water pressures, reflects the energy stored in the curved interface they share (equation 1.3). Because the equilibrium capillary pressure depends on the radius of curvature of the interface, one may bound the capillary pressure based on characteristic length scales of the porous medium. Sills *et al.* (1991) proposed the inequality:

$$P_c^{min} = \frac{2T}{R_c} \leq P_g - P_w \leq \frac{2T}{R_t} = P_c^{max}, \tag{2.17}$$

where R_c is the radius of a gas cavities and R_t is the critical pore throat radius within the grain-water matrix [55]. The mechanism captured by the lower bound is termed "cavity flooding" and implies that, if the capillary pressure becomes so low that it cannot support an interface with the minimum curvature of the gas voids, the water will imbibe into the cavity and pressurize the gas. The upper bound implies that, at high enough capillary pressures, the gas may invade into the tiny pore throats surrounding the large cavities. As mentioned in Chapter 1, R_c is likely so small that the upper bound would never be met in gassy sediments. Instead, during periods of rising gas pressure, the system would reach the plastic limit for cavity expansion before capillary invasion. These bounds could be expressed in terms of the horizontal gas effective stress by considering the horizontal water effective stress, $\sigma'_{hw} = \sigma_h - P_w$:

$$\sigma'_{hw} - P_c^{max} \leq \sigma'_{hg} \leq \sigma'_{hw} - P_c^{min} \tag{2.18}$$

Comparison with equation 2.14 show that these physical mechanisms imply the following plastic yield limits:

$$I = \sigma'_{vw} - P_c^{min} \tag{2.19}$$

$$C = P_c^{max} - \sigma'_{vw} \tag{2.20}$$

Because cohesion C is a property of the solid phase and has not been measured, we leave it as an unconstrained parameter to be tuned to the data. The cavity integrity

I has also not been measured, but we may speculate about its form. It is appealing to choose a cavity compression condition that would account for increased integrity with compression, as in equation 2.15. Instead of introducing two unconstrained parameters into the model, we instead choose a condition for cavity compression that may be constrained with limited system knowledge. We assume that cavity compression is triggered by the same limit as cavity flooding, or $I = \sigma'_{vw} - P_c^{min}$. If the elimination of gas-grain contacts with water flooding erodes the cavity structure more than the consolidation with decreased water pressure in the grain-water matrix, then this mechanism should be valid. The parameter P_c^{min} may be constrained, based a range of cavities of sufficient volume to impact gas release $R_c \in [100, 500]$ μm in equation 1.4, to $P_c^{min} \in [200, 1000]$ Pa. For an undrained response in deformable grains, the vertical (and therefore horizontal) water effective stresses reduce to a function of sediment depth, as will be explained in the next section on modeling elastic sediment response.

2.3.2 Elastic regime

A loaded solid deforms elastically if the displacements store potential energy in stretched molecular bonds so that the process is reversible and the energy recoverable upon unloading. In our model gassy sediments, an elastic response is predicted whenever the loading function f is strictly positive, so that the horizontal gas effective stress is between the cohesion and integrity limits (equation 2.14).

To predict the response to hydrostatic loading, we consider the undrained limit response. Here, the sediments are assumed so impermeable that the timescale for fluid flow be much longer than that of pressure variations [70, 69]. For nearly water-saturated sediments, this timescale may be approximated as:

$$t_{flow} = \frac{L}{u} \approx \frac{\mu_w(\phi c_f + c_m)L^2}{k}, \tag{2.21}$$

where c_f and c_m are the compressibilities of the fluid and drained solid matrix, respectively, weighted by porosity ϕ [53]. For the system of interest,reasonable estimates

for these values are $L \approx 1$ m, $\mu_w = 10^{-3}$ kg m^{-1} s^{-1}, $c_m \approx 6 * 10^{-7}$ Pa^{-1}, $\phi = 0.8$, and $k \approx 10^{-16}$ m^2 [56, 66]. If so, we find $t_{flow} \approx 50$ days, which is longer than the about daily variations in hydrostatic load on the sediment (Figure 1-3). If an undrained response approximates the system well at the timescale of interest, elastic pressure response of the fluid and matrix may be predicted with poroelasticity theory.

In an isotropic situation, or if $k_0 = 1$, the water pressure response to loading may be estimated using the mean stress, σ_m. The poroelastic coefficient weighting the fluid pressure response to mean stress is call the Skempton coefficient, B:

$$B \equiv \left. \frac{\partial P_f}{\partial \sigma_m} \right|_{\zeta=0}, \tag{2.22}$$

where ζ is the fluid content released, zero for an undrained response. This coefficient is between zero and one and is large when the compressibility of the fluid is small relative to the drained compressibility of the solid skeleton. When the individual solid grains are incompressible relative to the fluid or the skeleton, the results of Gassmann (1951) reduce to [18, 5]:

$$B = \left(\phi \frac{c_f}{c_m} + 1 \right)^{-1} \tag{2.23}$$

An equivalent poroelastic coefficient has been derived for jacketed loading situations, where a vertical load is applied and no horizontal deformation is permitted. The loading efficiency, γ, predicts the fluid pressurization with variations in vertical stress, σ_v:

$$\gamma \equiv \left. \frac{\partial P_f}{\partial \sigma_v} \right|_{\zeta=0} \tag{2.24}$$

During jacketed compression experiments, pure volumetric compression is supplemented by shearing action. The shear modulus of the sediment matrix helps to oppose the applied stress and remove some of the load from the fluid phase, so that $\gamma \leq B$. This can be seen by comparing equation 2.23 against equivalent expressions for γ in sediments saturated with a single fluid phase and with incompressible grains:

$$\gamma = \left(\phi \frac{c_f}{c_v} + 1 \right)^{-1}, \tag{2.25}$$

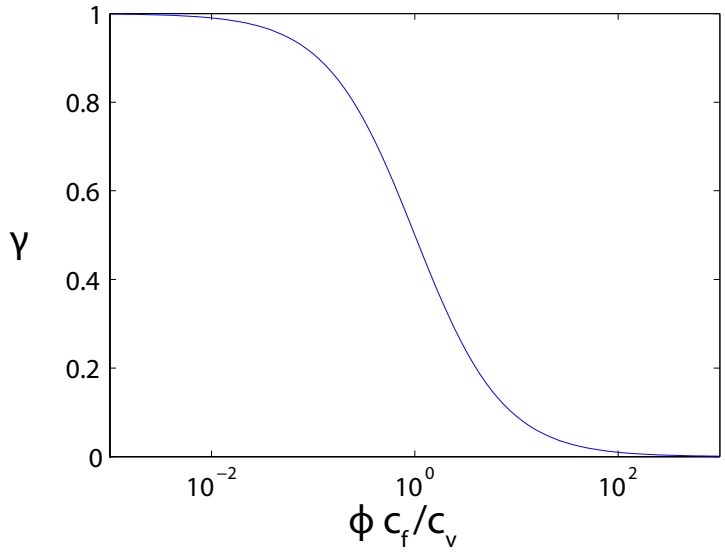

Figure 2-1: Loading efficiency γ vs. $\phi\frac{c_f}{c_v}$ on log scale. For highly-incompressible water, $\phi\frac{c_f}{c_v} \ll 1$ and $\gamma_w \approx 1$. For gas, literature values yield $\phi\frac{c_f}{c_v} < 0.1$, but experiments imply $\gamma_g = 0$.

where c_v is the jacketed, drained compressibility of the solid phase [69]. This jacketed compressibility may be related to the unjacketed one using the Poisson's ratio:

$$c_v = \frac{1+\nu}{3(1-\nu)} c_m \leq c_m, \tag{2.26}$$

where $c_v = c_m$ and $\gamma = B$ when $\nu = 0.5 \rightarrow k_0 = 1$ [30]. When $\nu = 3/7$, $c_v = 0.83 c_m$. The loading efficiency is plotted against $\frac{c_f}{c_v}\phi$ in Figure 2-1.

In gassy sediments, each fluid phase α may respond to loading with its own Skempton coefficient B_α and γ_α [9]. For water-saturated clay, $c_f = 4.8 * 10^{-10}$ Pa^{-1} for water and $c_m \approx 6 * 10^{-7}$ Pa^{-1} [56, 69], and equations 2.23 and 2.25 suggest that the Skempton coefficient and loading efficiency for water are both greater than 0.999.

Given this, perturbations in the total stress force equal changes in water pressure, and the water pressure remains is hydrostatic equilibrium. The water effective

stresses, σ'_{hw} becomes a constant function of sediment depth depth, z:

$$\sigma'_{hw}(z) = k_0\sigma'_{vw}(z), \tag{2.27}$$

$$\sigma'_{vw}(z) = \sigma_v(z,t) - P_w(z,t) = (\rho_b - \rho_w)gz, \tag{2.28}$$

$$\rho_b = (1-\phi)\rho_s + \phi\rho_w \tag{2.29}$$

where ρ_b is the bulk density, ρ_s the solid density, g the gravitational acceleration. Then the sediment integrity under compressibility also becomes a constant function of depth:

$$I(z) = \sigma'_{hw}(z) - P_c^{min}, \tag{2.30}$$

as long as P_c^{min} may be satisfactorily constrained.

We may estimate the gas pressure response during elastic deformation in two ways. The first method constrains gas pressure variations by assuming the presence of gas only increases the water compressibility - decreasing the water pressure sensitivity γ_w - and calculating the gas pressure from a saturation-capillary pressure curve [70, 71, 40]. This method is appropriate when gas bubbles remain trapped in existing pores, but the pore structure rearrangement with bubble growth in fine sediments invalidates a static drainage-imbibition curve. Alternatively, we could derive theoretical relationships for the Skempton coefficient and loading efficiency of the gas phase by simplifying lake sediments into a binary system of gas within a grain-water matrix:

$$B_g = \left(\frac{c_g}{c_m}\phi_g + 1\right)^{-1}, \tag{2.31}$$

However, the shear properties of the sediment-water matrix are affected by the morphology and distribution of gas cavities, making these expressions poorly constrained. Instead, we infer from the constant gas pressure during initial experimental unloading - the elastic regime before plastic yield - that the elastic sediment response does not strongly compress the gas cavities and that the gas loading efficiency γ_g may be approximated as zero (see Figure 2-2A, time period 3-4) [61]. We assume that the experimental results also apply to small hydrostatic variations in lake sediments, that

cavity compression is a purely plastic response.

2.3.3 Plastic regime

When the system reaches the limits of elastic behavior at $f(\sigma'_{hg}) = 0$, it deforms plastically according to a flow rule. For the one-dimensional loading function considered here, the flow rule reduces to enforcing gas pressure variations to satisfy $-C \leq \sigma'_{hg} \leq I$. Our model may be placed in the context of poromechanics theory, as outlined by [9]. The general form of the loading function (equation 2.11) constrains volume changes when $f = 0$:

$$df = \frac{\partial f}{\partial \boldsymbol{\sigma}} d\boldsymbol{\sigma} + \frac{\partial f}{\partial P_f} dP_f \geq 0, \tag{2.32}$$

which states that any change in the states $\boldsymbol{\sigma}$ and P_f must not cause the system to leave the feasible region by making f negative. In order to satisfy this, the plastic volume changes are restricted by the flow rules:

$$d\boldsymbol{\varepsilon}^p = d\lambda \frac{\partial f}{\partial \boldsymbol{\sigma}}; \quad d\phi^p = d\lambda \frac{\partial f}{\partial \phi}, \tag{2.33}$$

where $d\lambda$ is called the plastic multiplier and obeys the Kuhn-Tucker conditions:

$$d\lambda \geq 0; \quad f \geq 0; \quad d\lambda \cdot f = 0; \quad d\lambda \cdot df = 0 \tag{2.34}$$

In our model, the flow rules simplify due to the one-dimensional nature of the loading function (equation 2.13):

$$d\phi_g^p = d\epsilon^p = -d\lambda \text{sign}\left(\sigma'_{hg} + \frac{I - C}{2}\right), \tag{2.35}$$

so that the porosity rises during expansion and falls during compression. The magnitude of the contraction, $d\lambda$, is determined by the change in gas pressure dP_g required to constrain the horizontal gas effective stress between $-C$ and I, given a perturbation

$d\sigma_v$:

$$df = d\sigma'_{hg} = 0 \rightarrow dP_g = d\sigma_v \tag{2.36}$$

$$d\lambda = |d\phi_g^p| = \phi_g c_g dP_g, \tag{2.37}$$

where $c_g = P_g^{-1}$ for an ideal gas, a good approximation at near-standard conditions [34].

2.3.4 Synthesis

The combined elastic and plastic response of the model pressures is idealized in Figure 2-2 for a arbitrary depth within the sediment column. The left side of the figure (parts A-C) shows a schematic representation of the results from a drained loading and unloading experiment [61, 55], and the right side (D-F) demonstrates the model undrained response for the same loading and unloading path. The analysis figures B and C for the experiment are presented in terms of vertical stress because only those data were published, but the model analysis in D and E uses the horizontal stress. Both curves are parallel during an undrained response with $\gamma_w = 1$, as seen in subfigure D. The following compares the evolution in experiment and model.

The first row of subfigures shows the time evolution of stresses and pressures. The initial evolution between time points 0 and 1 is elastic, although this response is assumed to end instantly in the experiment. Time point 1 marks the onset of plastic cavity collapse. The vertical gas effective stress $\sigma'_{vg} = \sigma_v - P_g$ grows with increasing plastic compression in the experiment, but the model assumes I to be a constant function of depth within the sediment so that σ_{hg} remains constant during compression. This plastic deformation halts between time points 2 and 3, when the imposed stress is held constant. The water pressure continues to fall in the drained experiment, which allows the system to compress (C), but in the undrained model it has no outlet to diffuse the pressure buildup. During the initial unloading period (3-4), gas pressure remains constant in both the experiment and model because we assume $\gamma_g = 0$. Only at point 4, when the gas pressure reaches the sum of vertical

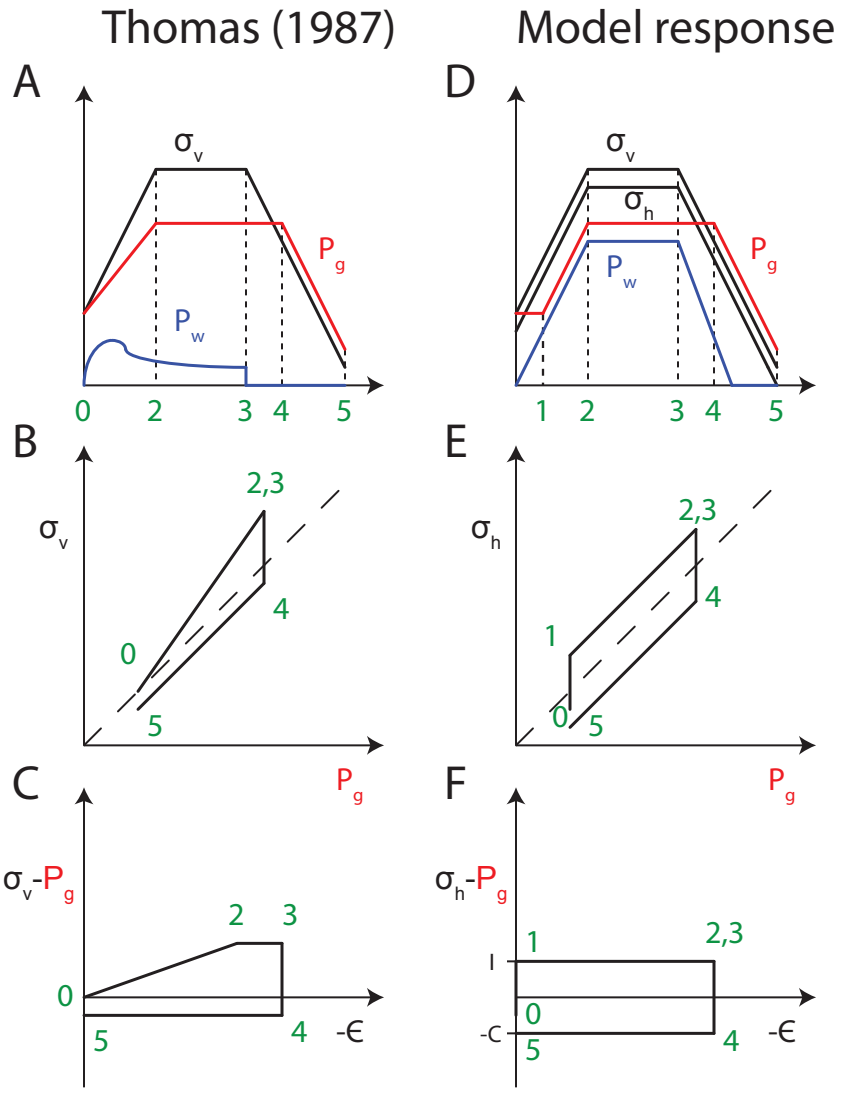

Figure 2-2: Idealizations of pressure and stress responses of gassy sediments. The left side shows the results from drained experiments by [61, 55], and the right side demonstrates the model response for an undrained experiment. A,D: time series of total vertical stress (black), gas pressure (red), and water pressure (blue). The six time indices in green correspond to (0) the initial condition, (1) beginning of plastic deformation (2) end of loading, (3) beginning of unloading, (4) onset of gas expansion, and (5) final condition. B,E: phase plane of vertical stress and gas pressure. C,F: horizontal gas effective stress σ'_{hg} versus compressive volumetric strain $-\epsilon$. See text for details.

stress and cohesion, does it begin to fall.

The second row of subfigures shows the phase plane of vertical stress and gas pressure. At left, the slope between 1 and 2 reflects increase in cavity integrity I during plastic cavity compression, which was tuned in the experimental interpretation as an empirical parameter [61]. This dynamic integrity is not captured by the model, which instead separates the compression into an elastic regime with slope $\gamma_g = 0$ and plastic one with constant slope due to constant I.

The stress-strain curves in the bottom row of highlight the utility of using an effective stress that includes the gas pressure to model the elastic-plastic system response. This horizontal gas effective stress is constrained at all times between limits I and $-C$, which are assumed constant in the model (F) but appear to vary with the loading state in experiments (C).

While the experiments above inform the nature of the sediment response over a single loading-unloading cycle, the nature of hydrostatic pressure variations on a lake sediment surface includes many cycles. Figure 2-3 shows the impact of measured hydrostatic pressure variations on the modeled vertical sediment stress, gas and water pressures at $z = 0.5$ m over a 15-day period. The top figure demonstrates the simplest case, a purely plastic response with $\gamma_g = C = P_c^{min} = 0$. Sandwiched between the water pressure and horizontal stress is the gas pressure, forced to rise during periods of cavity compression (and consequent volume reduction) and to fall when the cavities expand. Due to the highly-incompressible water and sediment grains, $\gamma_w \approx 1$ and the horizontal water effective stress $\sigma'_{hw} = \sigma_h - P_w$ remains constant for each depth (equation 2.28). Gray bars indicate periods when the plastic cavity expansion condition is met and conduits are dilated so that gas becomes mobile for upward flow, as will be addressed in the next section. The bottom figure demonstrates the model response with both elastic deformation ($\gamma_g = 0.7$) and plastic deformation with $C = P_c^{min} = 200$ Pa.

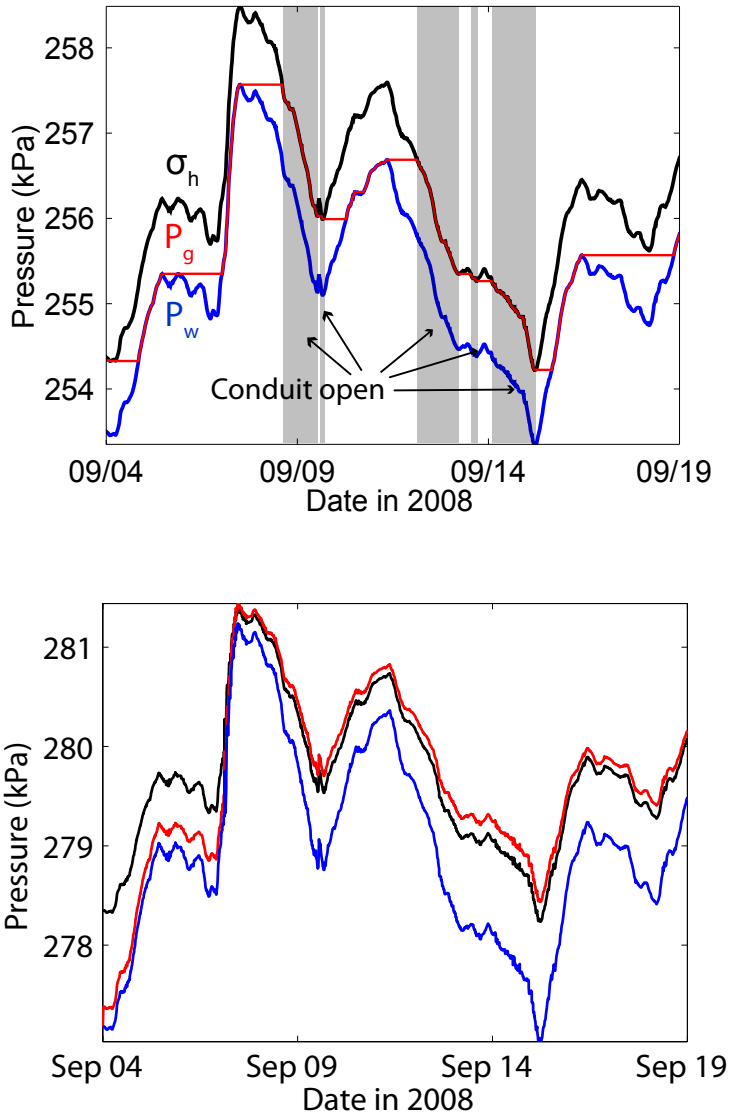

Figure 2-3: Evolution of horizontal stress (black), gas pressure (red), and water pressure (blue) at $z = 0.5$ m over 15 days of hydrostatic pressure variations. Top: plastic deformation only with $\gamma_g = 0$ and simple loading function limits $C = P_c^{min} = 0$ and lateral stress coefficient $k_0 = 1$. Shaded bars highlight periods where the cavity expansion condition is met and the flow conduits are open at that depth. Bottom: combined elastic and plastic deformation with $\gamma_g = 0.7$, $C = P_c^{min} = 200$ Pa, and $k_0 = 0.75$. The conduit is not necessarily open during periods of falling gas pressure, as in the top subfigure, but the open periods are not marked with shaded bars.

2.4 Escape: multiphase flow through dilated conduits

While the growth and development of trapped bubbles can be modeled with plastic and elastic poromechanics, their escape another mechanism. Instead of modeling the rise of a single bubble through sediments, we assume that the cavity expansion mechanism dilates a vertical conduit for free gas flow. These conduits may be preexisting and un-healed fractures, or new paths through non-cohesive sediments. Within a one-dimensional model domain, we assume that one vertical flow conduit may be opened by an expanding cavity at any depth and mobilize all the bubbles above that depth for rise to the surface. As in the poromechanics framework, the gas transport is treated as a continuum process, where fluxes of gas are predicted with equations for multiphase flow in porous media.

As gas-filled cavities expand due to excess gas pressure over sediment stress, they in essence dilate sub-vertical conduits through which gas may begin to flow. These conduits may be preexisting and un-healed fractures, or new paths through non-cohesive sediments. In the model, a conduit extends from the sediment surface to the maximum depth where gas pressure at least equals stress ($P_g \geq \sigma$), and gas and water are free to flow in that depth range (Figure 2-4(A)).

The mass balance for a species $i \in \{w, m\}$ for water and methane may be expressed as:

$$\frac{\partial m_i}{\partial t} + \nabla \cdot \boldsymbol{F}_i = g_i, \tag{2.38}$$

where m_i is the mass per control volume, $\boldsymbol{F}_i$ is the mass flux across control interfaces, and g_i is the rate of mass generation. The species mass may, in principle, partition over two phases $\alpha \in \{a, g\}$ for aqueous and gas, so that $m_i = \phi \sum_\alpha S_\alpha \rho_\alpha \chi_{i\alpha}$, where S_α is the volume fraction of phase α in the pore space, ρ_α the phase density, and $\chi_{i\alpha}$ the mass fraction of species i in α. However, we neglect dissolved transport of methane and have pure phases of aqueous water and gaseous methane: $\chi_{wa} = \chi_{mg} = 1$ and $\chi_{wg} = \chi_{ma} = 0$. Then the species masses become $m_w = \phi S_w \rho_w$ and $m_m = \phi S_g \rho_g$,

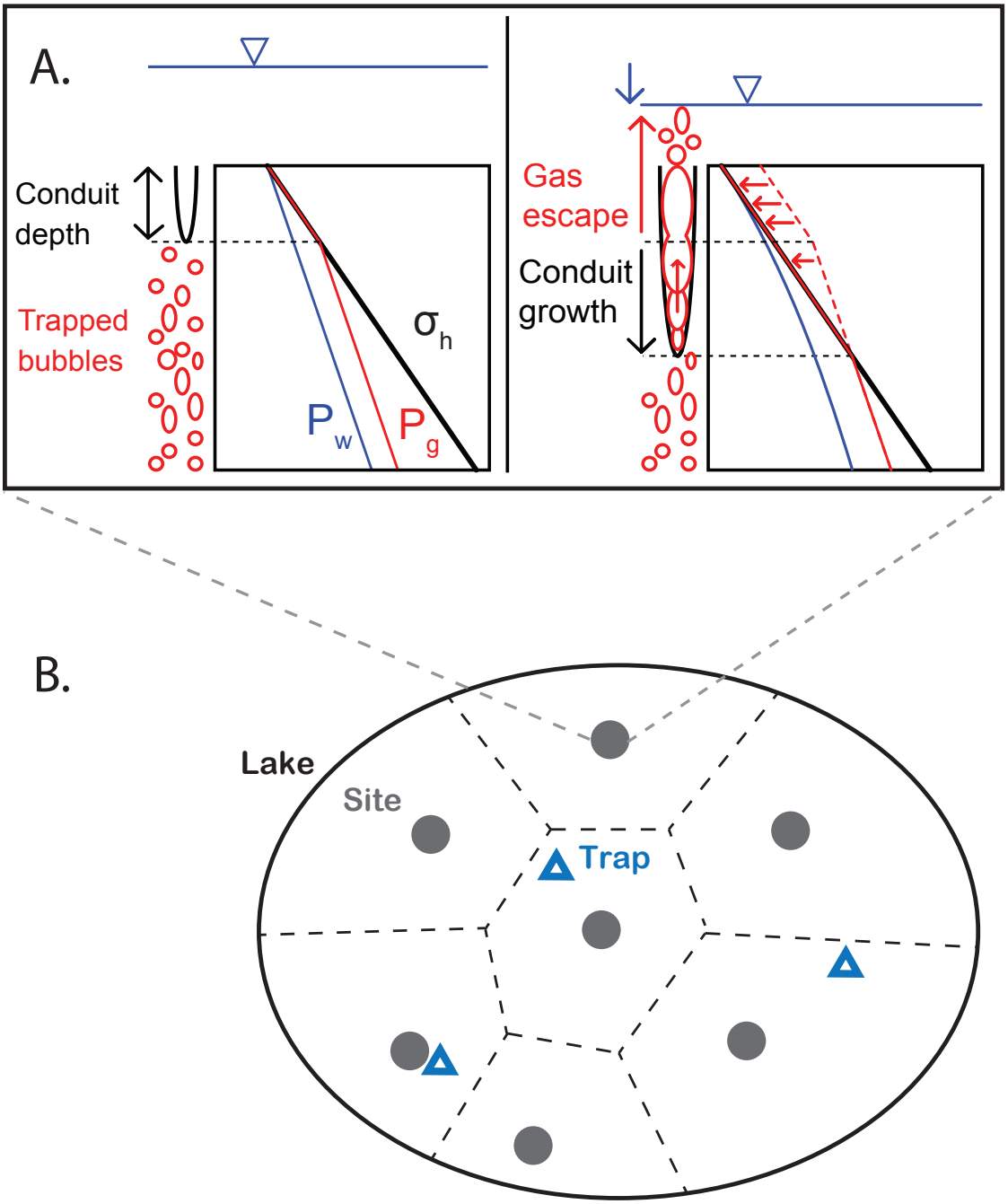

Figure 2-4: (A) Conceptual model for gas venting with water level drop. The left pane shows a lake overlying a sediment column with gas bubbles trapped for the entire depth where gas pressure P_g (red) is less than sediment stress σ_h (black). The right pane shows the impact of falling water level on σ_h, P_g and P_w (blue), and the opening of a gas-flow conduit to the depth where $P_g = \sigma_h$. (B) Plan view schematic placing 1D model venting sites (gray circles) within the sediment area, with randomly-placed bubble traps (blue triangles) at the lake surface.

where the saturations sum to one. Also, a general advection-diffusion expression for the mass flux F_i,

$$\boldsymbol{F}_i = \phi \sum_{\alpha} \left[v_\alpha \rho_\alpha \chi_{i\alpha} - D_{i\alpha} \nabla \left(\rho_\alpha \chi_{i\alpha} \right) \right], \tag{2.39}$$

reduces to

$$\boldsymbol{F}_w = \phi \boldsymbol{v}_w \rho_w, \quad \boldsymbol{F}_m = \phi \boldsymbol{v}_g \rho_g \tag{2.40}$$

To relate with the binary poromechanics framework above, we may express $\phi_\alpha = \phi S_\alpha$. When ϕ is large (measured above 80% in UML [66]) relative changes in gas saturation $S_g < 10\%$ are much larger and porosity variations may be neglected. We further assume that all changes in gas pressure and density are accounted for by the poromechanics evolution, so that the only role of flow through porous media is volume translation. In this case the mass balance for the gas phase simplifies to

$$\frac{\partial S_g}{\partial t} + \nabla \cdot \boldsymbol{v}_g = G_g, \tag{2.41}$$

where $G_g = g_g/(\phi \rho_g)$. We adopt Muskat's multiphase extended form of Darcy's law [47] to describe the gas velocity:

$$\boldsymbol{v}_g = -\frac{k k_{rg}}{\phi \mu_g} \left(\nabla P_g - \rho_g \boldsymbol{g} \right) \tag{2.42}$$

where k is the intrinsic permeability, k_{rg} the gas relative permeability (assumed equal to saturation S_g), μ_g the gas viscosity, and $\vec{g}$ the gravitational constant vector, pointing downward with z. The density of methane may be estimated using the ideal gas equation of state:

$$\rho_g = \frac{m}{V} = \frac{P_g}{RTM}, \tag{2.43}$$

which states that the ratio of gas mass m to volume V is proportional to the ratio of pressure P_g to the product of the gas constant R, temperature T, and molar mass M [34]. At conditions characteristic of UML sediments, the gas density ranges from 1-3 kg m^{-3}. The gas velocity v_g is used both to evolve the saturation equation (2.41) and to predict the flux of gas from the sediments into the water column above.

Given an initially-hydrostatic water pressure profile within the sediment and a loading efficiency of $\gamma_w = 1$, the water pressure remains in hydrostatic equilibrium even with perturbations in the hydrostatic load on the sediment surface. The water velocity according to Muskat's extended Darcy's law then equals zero everywhere:

$$\boldsymbol{v}_w = -\frac{k k_{rw}}{\phi \mu_w} \left(\nabla P_w - \rho_w \boldsymbol{w} \right) \tag{2.44}$$

In fact, some water is entrained by gas bubbles rising through sediments, but such momentum-transfer effects are not captured by this multiphase expression. Laboratory experiments suggest that the volume ratio of entrained water to gas by bubbles rising through fine sediments is less than 0.1 [33]. This, combined with the low methane solubility of lake water, suggests that transport of dissolved methane in entrained water may be safely neglected.

The flow equations may be nondimensionalized to reduce the number of unconstrained parameters, and this is especially convenient when the gas relative permeability is proportional to the gas saturation. In one dimension, equation 2.41 may be normalized by G_g and made dimensionless using a characteristic time t^* and length scale h:

$$\frac{\partial \bar{S}}{\partial \bar{t}} + \frac{\partial}{\partial \bar{z}} \left(\bar{S} \bar{v_g} \right) = 1, , \tag{2.45}$$

where $\bar{S} = S_g / (G_g t^*)$ is the dimensionless accumulated methane exsolution time (shown on the left side of Figure 2-6), $\bar{t} = t/t^*$ is dimensionless time, and $\frac{\partial}{\partial \bar{z}} = h \frac{\partial}{\partial z}$ is a dimensionless vertical gradient. This equation is then solved on the domain $z \in [0, 1]$ instead of $[0, h]$. The dimensionless velocity, $\bar{v_g}$, is defined:

$$\bar{v_g} = \frac{v_g t^*}{S_g h} = -\alpha \left(\frac{\partial}{\partial \bar{z}} \left(\frac{P_g}{P^*} \right) - \frac{\rho_g}{\rho_w} \right), \tag{2.46}$$

$$\alpha = \frac{k \rho_w g t^*}{\mu_g \phi h} \tag{2.47}$$

$$P^* = \rho_w g h \tag{2.48}$$

where α is the characteristic dimensionless velocity, the number of t^*s required for

a burp of gas to rise from depth h to the sediment surface. The dimensional time required for this traverse is α/t^*. While we could define $t^* = G_g^{-1}$ so that $\bar{S}$ would equal the physically-understood gas saturation, S_g, leaving these two independent allows us to estimate the unconstrained generation rate while comparing against data referenced to real, dimensional time. The dimensionless flux,

$$\bar{F}_g = \bar{S}_g \bar{v}_g = \frac{\phi v_g}{\phi h G_g}, \tag{2.49}$$

is exactly what we need to predict the atmospheric flux using constrained parameters, as described below in Section 2.5. Instead

Combining equations 2.45 and 2.46, we see that the saturation equation would have the form of the hyperbolic, first-order wave equation

$$\frac{\partial \bar{S}_g}{\partial \bar{t}} + \alpha \frac{\partial \bar{S}_g}{\partial \bar{z}} = 1, \tag{2.50}$$

if the normalized gas pressure gradient was constant and equal to one. The ratio of gas to water densities in equation 2.46 is less than 0.003 so may be neglected. Averaged over the model domain, the gas pressure gradient should be constrained by the water pressure and horizontal stress gradients so that

$$1 \leq \frac{\partial}{\partial \bar{z}} \left(\frac{P_g}{P^*} \right) \leq \frac{\partial_z \sigma_h}{\partial_z P_w} = k_0 \left[(1-\phi) \frac{\rho_s}{\rho_w} + \phi \right] + (1 - k_0) \approx 1.3, \tag{2.51}$$

where the first equality is derived from equations 2.29 and 2.9, and the given estimate assumes $k_0 = 0.75$, $\phi = 0.8$, and $\rho_s/\rho_w = 2.7$. Of course, the gradient may vary outside of these bounds to some extent, due to local gas pressure variations, and cause local gas accumulation, So, we integrate the full dimensionless equation 2.45 rather than the approximate equation 2.50. The flow equations are discretized with a secund-order finite volume scheme using linear reconstruction and a monotized central limiter [65]. They are integrated over each time step with a second-order Runge-Kutta method, following the poromechanical evolutions in a staggered manner. The numerical grid is the same for both poromechanics and flow, with 64 control volumes

in the vertical direction so that the height of an REV is on the cm scale. No flux is allowed across the bottom boundary or at any depth below the bottom extent of the open conduit. The gas pressure at the top of the conduit is assumed hydrostatic, and a natural outflow boundary condition is imposed at the sediment surface. The gas flux $v_g(z = 0)$ out the top of the domain is used to estimate the atmospheric flux by placing the one-dimensional model within context of a physical lake.

2.5 Bubble rise through the free water column

The combination of gas generation, cavity compression and flow through conduits allows our model to predict volumetric fluxes of gas at the sediment surface based on input hydrostatic pressure variations. These mechanisms are validated by comparing the flux history against four months of ebullative flux measurements taken at UML by bubble traps [67]. The record from five traps placed effectively randomly on the lake surface is taken to represent the lake-wide ebullative atmospheric flux. In fact, the strong episodicity and spatial concentration of venting events means that this record likely misses some large venting events [68], but the spatiotemporal complexity of the signal should capture much of the important release dynamics [66]. Because the flow model output is volumetric gas flux at the sediment surface but the data are collected at the lake-atmosphere interface, our model must specify what happens to the gas volume during rise through the water column.

As seen in Figure 1-2, both sediment gas accumulation and ebullition are concentrated into distinct areal pockets. Our model neglects the lateral transport mechanisms probably required to form and maintain gassy sediment pockets, but it does account for spatial concentration of the exsolution and release processes. The one-dimensional model venting site is assumed to have identical clones scattered uniformly over the sediment surface, as shown in Figure 2-4(B). The relationship between the flux F^{sed} of gas volume per active venting sediment area predicted by our model, and

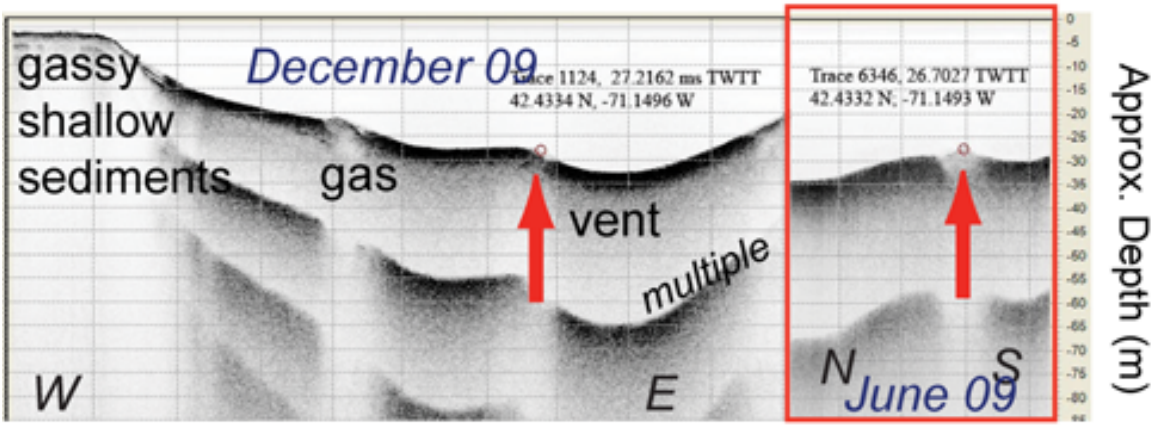

Figure 2-5: Seismic surveys of UML sediments in June and December, 2009, showing persistence of a venting site.

lake surface flux F^{atm} that the bubble traps measure, may be expressed as:

$$F^{atm} = \bar{D}\bar{A}F^{sed}, \tag{2.52}$$

$$F^{sed} = \phi v_g(z = 0), \tag{2.53}$$

where $\bar{D}$ is the ratio of individual bubble volumes at the lake and sediment surfaces, $\bar{A} = A^{vent} * n^{vent}/A^{sed}$ is the fraction of the sediment surface covered by venting sites. The bubble volume ratio $\bar{D}$ should be closer to one during periods of vigorous venting, when upwelling currents and local methane saturation inhibit dissolution [37, 19]. However, Figure 1-6(top) suggests that it should depend strongly on the bubble sizes, a yet unconstrained parameter. As a first approximation, we assume a distribution of bubble diameters centered around 4 mm so that $\bar{D}$ is a constant approximately one.

The areal ratio $\bar{A}$ accounts for the spread of a bubble plume during rise, or from a statistical perspective that the expected flux captured by randomly-placed point-sized bubble traps is proportional to the density and area of influence of individual venting sites. The active areal fraction could change as venting sites become active or dormant by accumulating excess bubble volume or exhausting their stores. However, repeated surveys of UML sediments in June and December, 2009 (Figure 2-5) detected a pocket

of gassy soil at the same location, implying that these features may be persistent on the annual scale of interest. Inspection of Figure 1-2 suggests that the vent spacing may be on the order of 100 m so that $\bar{A} \approx 10^{-4}$, but the use of a normalized model allows us to eliminate this poorly-constrained parameter.

Because the flow equations assume incompressible fluids, the bubble rise within the sediment does not feed back to the conduit opening or closing conditions. Information flows only one direction, from the hydrostatic pressure forcing, to the poromechanical evolutions, to the conditions to open or close flow conduits, to the rate of gas flux into the water column and atmosphere. Experiments and physical reasoning suggest that, once a gas bubble becomes mobile within the sediment, it will rise all the way to the sediment surface [4]. Our model has no self-reinforcing mechanism to ensure this behavior. Instead, a "burp" of gas may be mobilized by a deepening conduit during a period of hydrostatic pressure drop, only to be trapped again higher in the sediments by a rebound in the hydrostatic pressure forcing. This behavior can be seen in Figure 2-6, where a burp is mobilized (top) and then trapped (bottom).

2.5.1 Cumulative release tuning

When bubble flux attenuation between the sediment and atmosphere by dissolution and spreading is assumed constant, we may eliminate the unconstrained parameters $\bar{D}$, $\bar{A}$, and G_g using the seasonally-integrated measured bubble flux. This is because the entire model then becomes linear in gas saturation when the relative permeability is also linear ($k_{rg} = S_g$). The seasonally-averaged flux at the sediment and atmosphere,

$$\tilde{F}^{atm} \equiv \frac{1}{t_f - t_i} \int_{t_i}^{t_f} F^{atm} dt, \tag{2.54}$$

$$\tilde{F}^{sed} \equiv \frac{1}{t_f - t_i} \int_{t_i}^{t_f} F^{sed} dt, \tag{2.55}$$

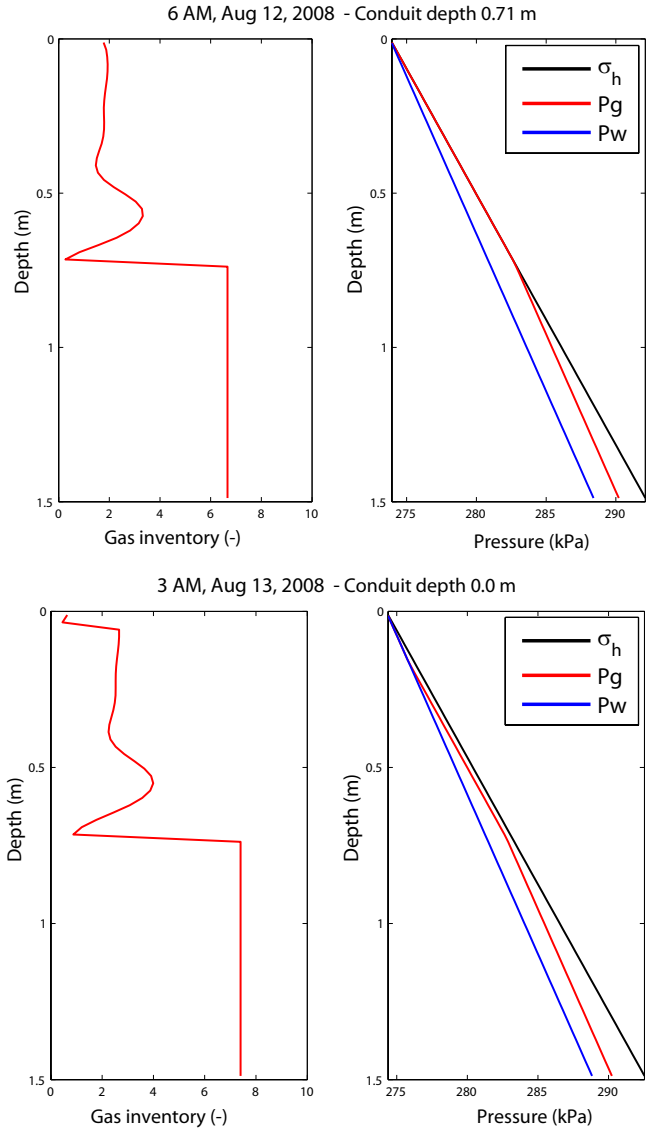

Figure 2-6: Depth profiles of gas volume (left) and pressures (right) for two instants in time: (top) a burp of gas at 0.55 m in the sediment is mobilized by a the deepening flow conduit, but the same burp becomes trapped an hour later as the conduit shallows with a rising hydrostatic pressure input (not shown). The next day (bottom), the horizontal stress has risen noticeably and kept the gas burp trapped at depth even as it grows with the uniform exsolution rate, G_g. In these simulations $C = P_c^{min} = 0$ so that gas pressure is constrained between the water pressure and horizontal stress. The sediment permeability, k, is $5 * 10^{-14}$ m^2 ($\alpha \approx 2$), and such trapped bubbles would not occur frequently in higher-permeability sediments where the bubble rise time is shorter (larger α). The gas inventory is normalized saturation $\bar{S}_g$.

are related by $\tilde{F}^{atm} = \bar{D}\bar{A}\tilde{F}^{sed}$,when $\bar{D}$ and $\bar{A}$ are constant. These are further related to the average volume generation rate per venting site area by:

$$\tilde{F}^{gen} \equiv \frac{1}{t_f - t_i} \int_{t_i}^{t_f} \int_0^d \phi h G_g dz dt = \phi d G_g, \tag{2.56}$$

where the second equality holds true when the generation rate and porosity are constant and uniform over the depth of methane-generating sediments, h. The integrated sediment flux and areal generation are related by

$$\bar{R} \equiv \frac{\tilde{F}^{sed}}{\tilde{F}^{gen}}, \tag{2.57}$$

where $\bar{R} = 1$ if the system is at steady-state between t_i and t_f. The atmospheric flux is related to the generation rate by

$$\tilde{F}^{atm} = \bar{D}\bar{A}\bar{R}\phi h G_g, \tag{2.58}$$

which may be estimated using the integrated bubble trap data in equation 2.54. This atmospheric flux, averaged over five bubble trap records with continuous continuous monitoring from August eighth to December first, 2008, is $\tilde{F}^{atm} = 27$ mL m^{-2} day^{-1}. Then the product

$$\tilde{G} = \bar{D}\bar{A}\phi h G_g = \frac{\tilde{F}^{atm}}{\bar{R}} \tag{2.59}$$

is the effective areal exsolution rate at the lake surface. If we can assume a value for $\bar{R}$, $\tilde{G}$ is estimated by the average trap data, and equation 2.52 shows it may be used to model the atmospheric flux:

$$F^{atm} = \bar{F}_g \tilde{G}, \tag{2.60}$$

$$\bar{F}_g = \frac{F^{sed}}{\phi h G_g}, \tag{2.61}$$

where equations 2.49, 2.53, and 2.61 confirm that the desired flux $\bar{F}_g$ is the output of the dimensionless saturation equation 2.45.

Owing to this simplification, we could imagine two extreme cases that our model treats as equivalent. In the first, rapid gas generation creates large saturations and release rates that are concentrated on a small fraction of the sediment surface. In the second case, lower generation rates are spread more evenly over the whole area, creating lower gas saturations and sediment fluxes. In both cases the atmospheric fluxes F^{atm} and parameter $\tilde{G}$ are identical. It should be reiterated that this simplification allows us to constrain the product including $\bar{D}$, $\bar{A}$, and G_g only when they are all assumed constant. This should not remain the case for dynamic dissolution mechanisms, to be considered in future work. For a first attempt the parameter constraint is appealing because it only requires extra input data and not explicit tuning. In general we assume steady state to estimate $f^{atm} \approx \tilde{F}^{atm}\bar{F}_g$ and measure $\bar{R}$ from the fraction of methane generated that is released by the model into the water column. $\bar{R}$ can be distilled from equations 2.57, 2.56, and 2.61 in terms of $\bar{F}_g$:

$$\bar{R} = \frac{1}{\bar{t}_f - \bar{t}_i} \int_{\bar{t}_i}^{\bar{t}_f} \bar{F}_g d\bar{t} \tag{2.62}$$

However, one can also use the above equation to tune $\bar{R}$ without any knowledge of $\tilde{F}^{atm}$, in which case $\tilde{G}$ is constrained and the seasonal cumulative model gas release matches the data exactly. Sensitivity analysis and results will specify in each case whether $\bar{R}$ is treated as a tuned input or a measured output.

The model presented above may be used to simulate methane ebullition from lake sediments in response to hydrostatic pressure variations. In modeling gas volume generation, bubble evolution and release, a number of unconstrained parameters were introduced. The following chapter analyzes the model sensitivity to these parameters.

Table 2.1: Summary of parameters and constants, including the method or source used to constrain them.

Parameter	Name	Units	Range	Constraint method
α	characteristic velocity	-	0.1-100	model tuning
k	intrinsic permeability	m^2	$10^{-14} - 10^{-12}$	model tuning (α)
h	active sediment height	m	0.5-3	model tuning
C	sediment cohesion	Pa	0-5000	model tuning
P_c^{min}	minimum capillary pressure	Pa	200-500	tuning, [55, 54]
$\bar{R}$	release ratio	-	$0 - 1$	model tuning
$\tilde{F}^{atm}$	average surface flux	mL m^{-2} day^{-1}	27	[66]
d_0	mean water depth	m	10-25	[66]
ϕ	porosity	-	0.8-0.95	[66]
k_0	lateral stress coefficient	-	0.74-0.76	[61]
μ_w	water dynamic viscosity	kg m^{-1} s^{-1}	$1.8 * 10^{-3}$	[34]
μ_g	gas dynamic viscosity	kg m^{-1} s^{-1}	$1.7 * 10^{-5}$	[34]
ρ_w	water density	kg m^{-3}	1000	[34]
T	sediment temperature	$^\circ$ C	4-6	[66]
R	ideal gas constant	J K^{-1} mol^{-1}	8.314	[34]
M	methane molecular mass	g mol^{-1}	16	
γ_w	water loading efficiency	-	1	[56, 69]
γ_g	gas loading efficiency	-	0	[61, 55]

Chapter 3

Model Sensitivity

This chapter investigates the model sensitivity to the primary unconstrained parameters. Except where otherwise noted, the model is run from August 6 to December 1, 2008, and the cumulative release volumes and fluxes are averaged to the day.The default parameter values are: $h = 1.5$ m, $P_c^{min} = C = 0$, and $\alpha = 4 \leftrightarrow k = 10^{-13}$.While much of the interesting model dynamics occur at the sub-daily timescale, the research goal is to match the daily gas flux record from the bubble traps. So, most of the sensitivity analysis is presented in terms of daily fluxes, while future work will focus on finer temporal resolution.

3.1 Model height

Figure 3-1 shows the model sensitivity to h, the height of the sediment column that is actively generating and releasing methane. When $h = 1$, the flow conduit frequently opens throughout the entire model domain and empty the venting site of its accumulated methane volume, so that 98% of the methane generated is released ($\bar{R} = 0.98$). For a deeper model $h = 2$, the conduit reaches the bottom less frequently and only 88% of the methane exsolved is released. However, the storage of methane out of reach of small hydrostatic pressure perturbations allows greater cumulative release during these extreme pressure drop events, as near September 29. Figure 3-2 shows that this large gas release is not due to a faster flux rate, but because the source of

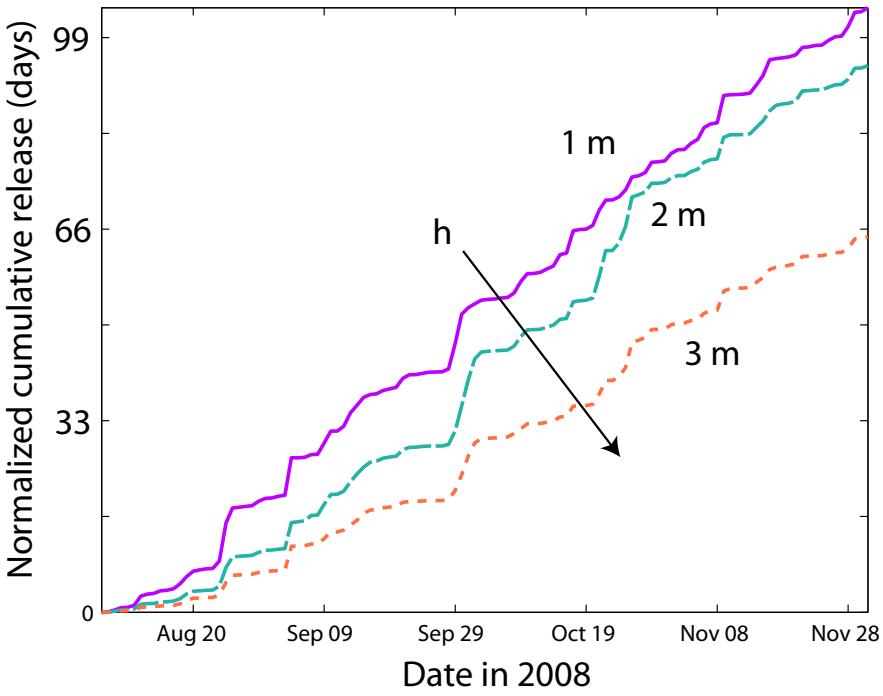

Figure 3-1: Cumulative methane volumes released to the atmosphere from model sediments for sediment column heights $h = 1$, 2 and 3 m. For increasing active sediment depth given the same areal generation rate estimated from the data, the volume released is less because the conduit does not open through the entire model depth and the bubbles take longer to rise.

methane takes longer to be depleted so that the flux peak is wider. These trends continue for an even deeper model ($h = 3$), which keeps nearly 40% of the generated methane trapped because so much of the model is inaccessible to the gas conduit given hydrostatic head variations of less than half a meter (equivalent to ~ 5 kPa). At this point the assumption of a steady state inventory of gas over the season ($\bar{R} = 1$) for estimating $\tilde{G}$ is no longer valid, and the generation rate G_g would have to be tuned considering this long-term methane storage.

3.2 Conduit permeability

The intrinsic permeability k is the least-constrained part of the derived flow parameter α, defined in equation 2.47. The dimensional k reflects the ease with which fluids

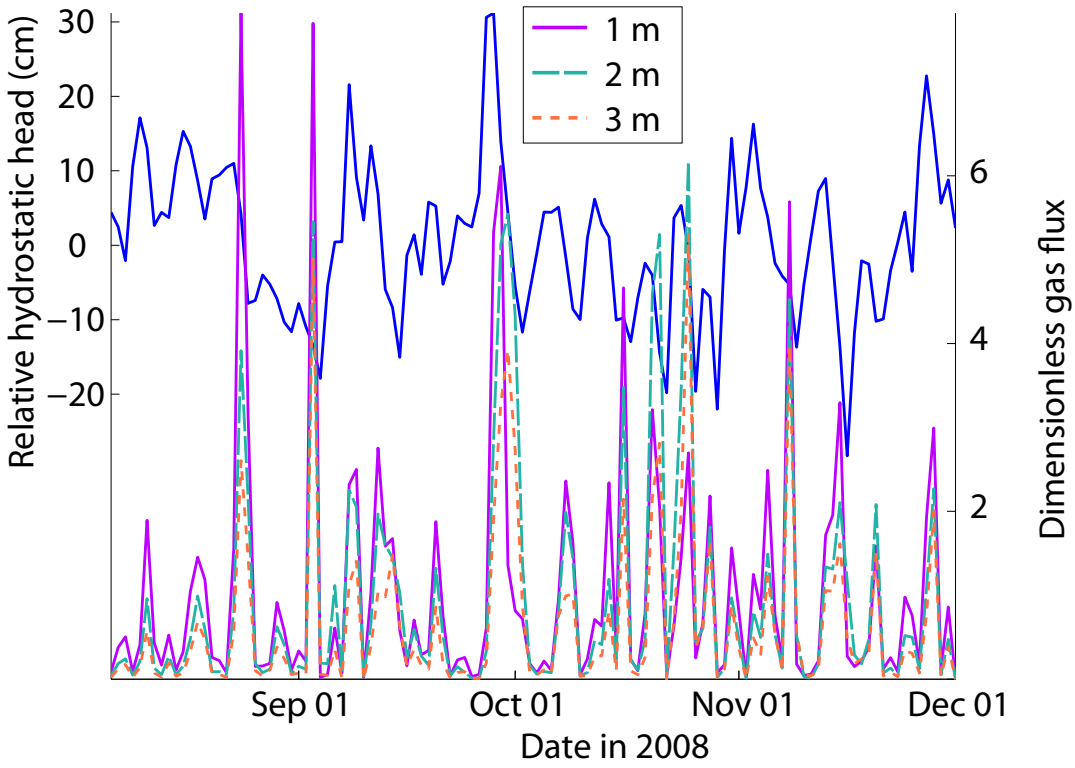

Figure 3-2: Model methane fluxes for three sediment column heights $h = 1$, 2 and 3 m. The left axes and solid blue line show the model input, hydrostatic pressure variations (in terms of cm water head), and the right axes show the scale of gas fluxes. For increasing h the initial peak magnitudes are smaller (*e.g.* August 25^{th}), but the model continues to release methane for longer during extreme pressure drop events like near October first and reaches higher peak flux rates during repeated pressure drop events in mid-October, when the shallow model ($h = 1$) is relatively depleted.

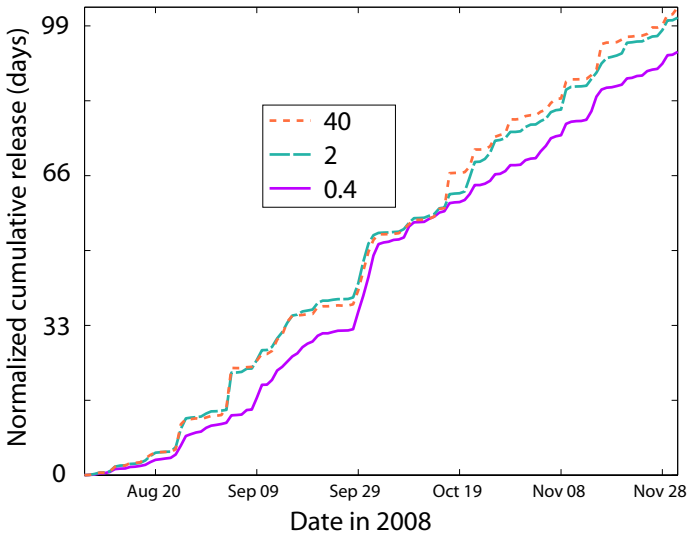

Figure 3-3: Cumulative methane volumes released to the atmosphere from model sediments for dimensionless velocities $\alpha = 0.4, 2$, and 40. These correspond to open-conduit permeabilities $k = 10^{-14}, 5 * 10^{-14}$, and 10^{-12} m^2. More methane is released from more permeable conduits, although increasing α past 2 has little impact on the cumulative release because the characteristic release time is reduced below 12 hours.

are transported vertically out of the venting site, and in the context of our model gassy sediments it should capture both the aperture of the flow conduits and an unspecified lateral gas transport mechanism that transfers bubbles into the conduits. The characteristic dimensionless time for a gas bubble to rise through the sediments is α^{-1}, and the dimensional time is t^*/α. Comparison with the data was easiest using $t^* = 3600 * 24$ seconds, or one day in SI units. So, when $\alpha > 1$, the timescale for release is less than a day, and the releases are essentially instantaneous at the daily timescale (Figures 3-3 and 3-4). The current work focuses on matching the daily release record, however future work on capturing the spatiotemporal concentration of ebullition will require higher-frequency modeling that should be sensitive to values of $\alpha > 1$.

Low values of α may delay the methane release, attenuate the flux rate, or prevent a gas burp from reaching the sediment surface at all. This last case, of gas mobilized and then re-trapped, is exhibited in Figure 2-6. For values of $\alpha > 1$, hourly resolution is required to visualize the difference in flux records, as shown in Figure 3-5. The

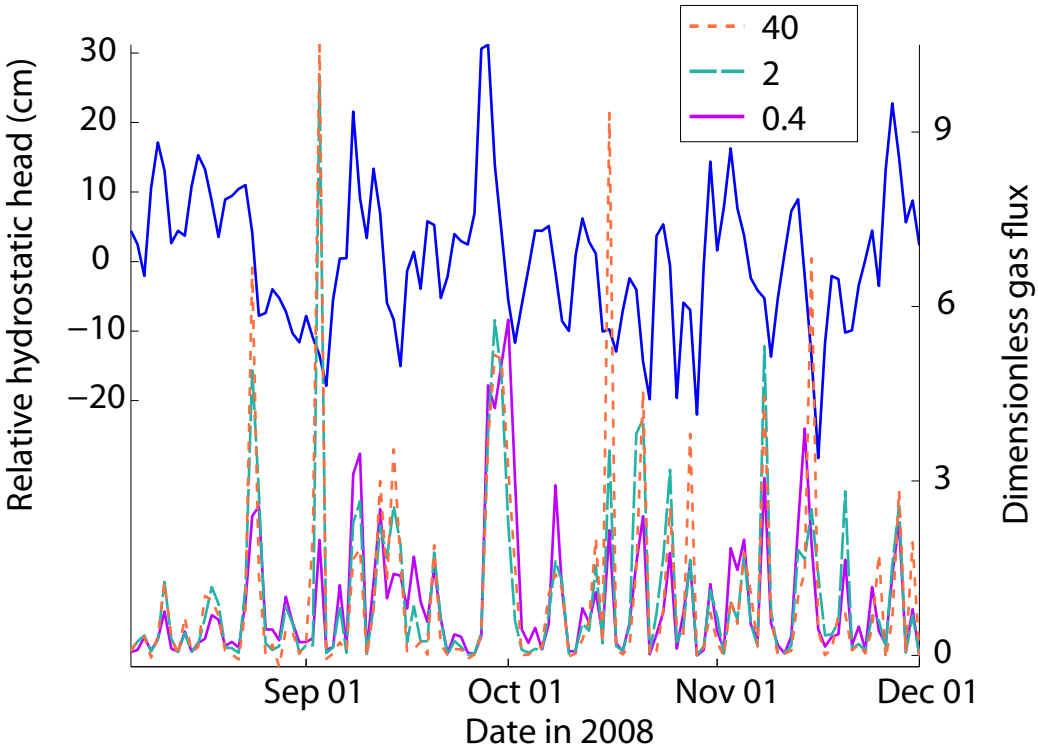

Figure 3-4: Daily-average model methane fluxes for three dimensionless velocities $\alpha = 0.4, 2$, and 40, corresponding to permeabilities $k = 10^{-14}, 5 * 10^{-14}$, and 10^{-12} m^2. The two higher-permeability models exhibit much sharper peaks during the maximum August and September ebullition events. The lower-permeability model maintains a high flux rate during the October first event because it takes time for the bubbles to rise to the sediment surface, while the higher-permeability models evacuate their inventories instantaneously on the daily time scale. Higher temporal resolution is required for the model to be sensitive to alpha values above 1.

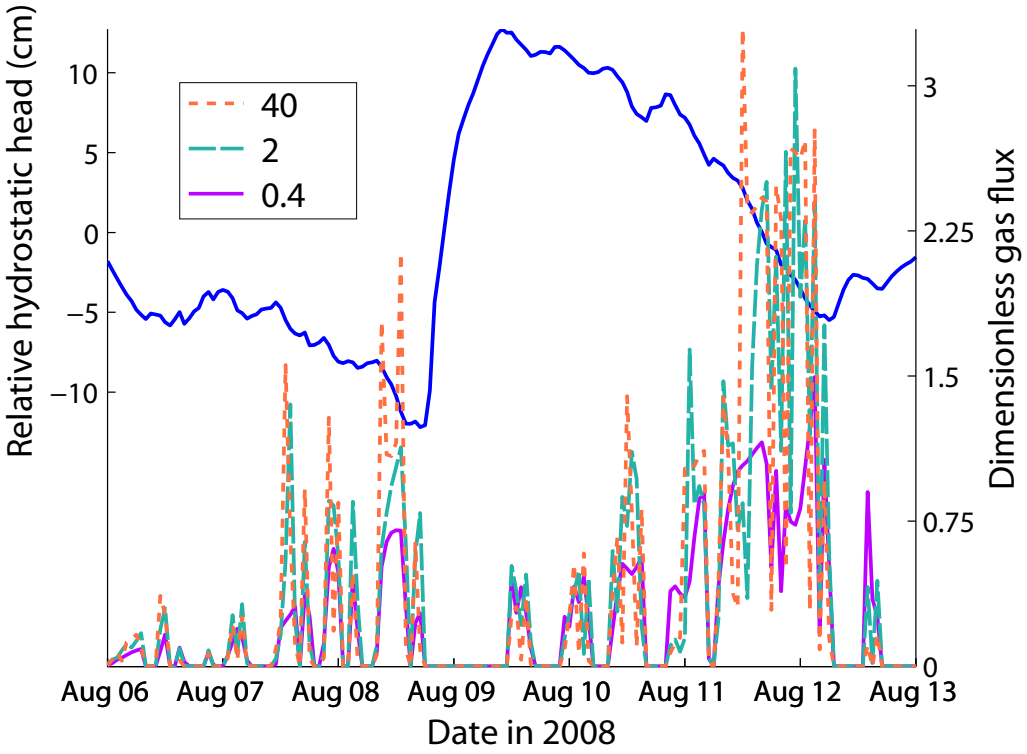

Figure 3-5: Hourly-average model methane fluxes for three dimensionless velocities $\alpha = 0.4, 2$, and 40. More conductive models have sharper peaks and greater cumulative releases (Figure 3-3).

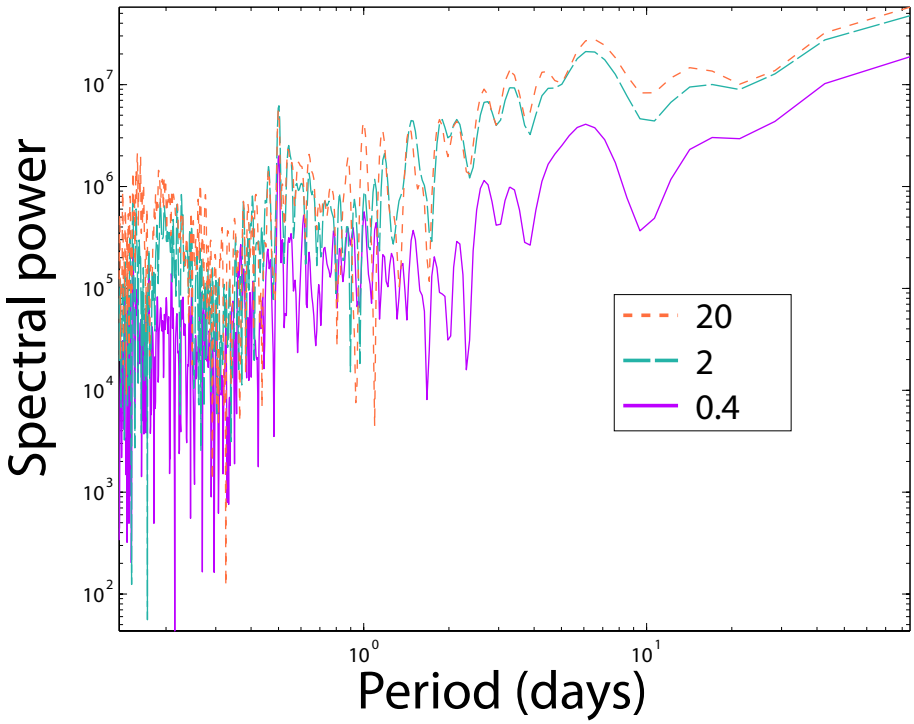

Figure 3-6: Power spectra for an hourly-resolution simulation from August 6 to September 1, with $\alpha = 0.4, 2$, and 20, corresponding to $k = 10^{-14}, 5 * 10^{-14}$, and $5 * 10^{-13}$ m^2.

$\alpha = 0.4$ model has both lower flux values and smoother peaks compared with the more conductive models. The impact of conductivity may be visualized with the power spectrum of the signal (the squared magnitude of the Fourier transform), shown in Figure 3-6. Larger α values increase the power at most frequencies. Not only is more methane released, but the portion of the signal from high-frequency (small-period) components is higher because individual burps of gas may evacuate the sediment column faster, shortening the flux event.

3.3 Plastic limits

The two plastic deformation coefficients left unconstrained in Chapter 2 are the sediment cohesion, C, and minimum capillary pressure, P_c^{min}. Increasing cohesion tends to inhibit ebullition, while increasing the minimum capillary pressure encourages it,

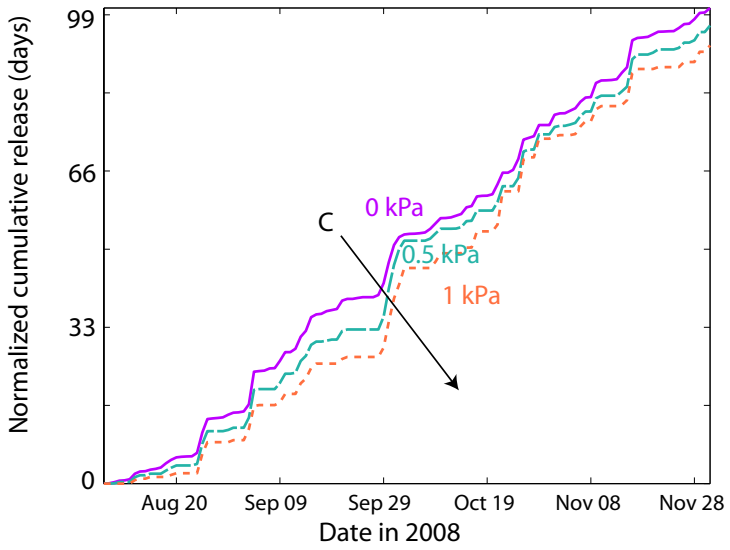

Figure 3-7: Cumulative methane volumes released to the atmosphere from model sediments for cohesion $C = 0, 0.5$, and 1 kPa. Increased cohesion demands a greater hydrostatic pressure drop to initiate conduit flow, but once open the conduit emits larger bursts of gas Figure 3-8. As can be seen from the different seasonal cumulative releases, the values of $\bar{R} = 95, 91$, and 88% were not used to match the seasonal data.

as explained below.

3.3.1 Cohesion

The influence of nonzero sediment cohesion on the gas pressure evolution may be seen in Figure 2-3. Cohesion allows the sediment stress to drop below the gas pressure during hydrostatic unloading, delaying or preventing the release from a given depth. So, the cumulative release record in Figure 3-7 is smaller for more cohesive sediments. However, the gas stored at depth during minor events may still be released during major events so that the distribution of mean flux rates per event is more highly weighted to large fluxes (Figure 3-8).

3.3.2 Minimum capillary pressure

While sediment cohesion tends to delay or inhibit ebullition by requiring larger-magnitude hydrostatic pressure drops, the minimum capillary pressure has the op-

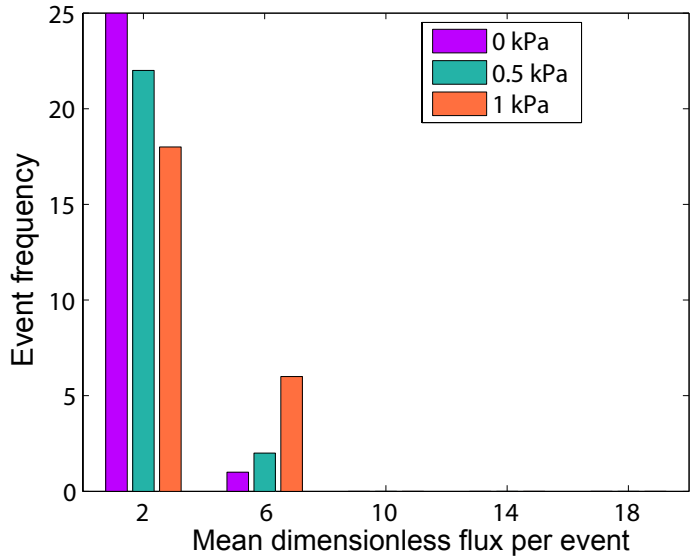

Figure 3-8: Histogram of average gas flux rate per event (period with daily flux rate above 15 mL m^{-2} day^{-1}) for cohesion $C = 0, 0.5$, and 1 kPa. More cohesive sediments release more of their gas in temporally-concentrated bursts.

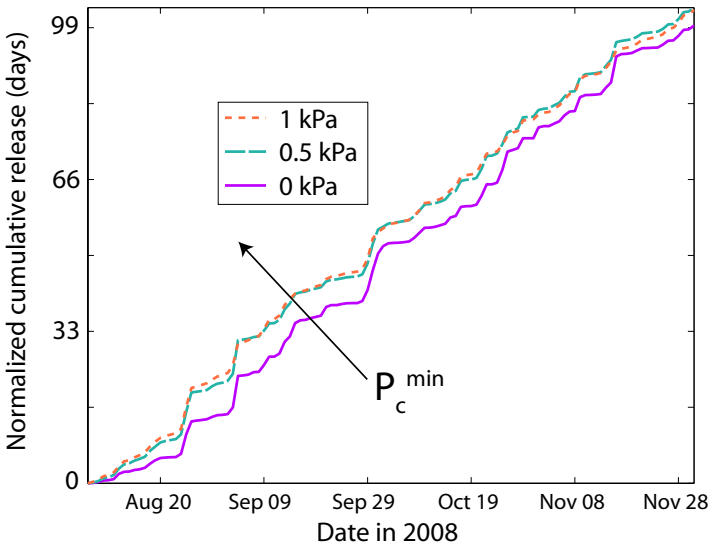

Figure 3-9: Cumulative methane volumes released to the atmosphere from model sediments for minimum capillary pressures $0, 0.5$, and 1 kPa. Increasing this minimum capillary pressure forces the gas pressure higher during periods of rising hydrostatic pressure, and these high gas pressures trigger earlier and more frequent conduit opening. The cumulative release record then stays closer to a straight line.

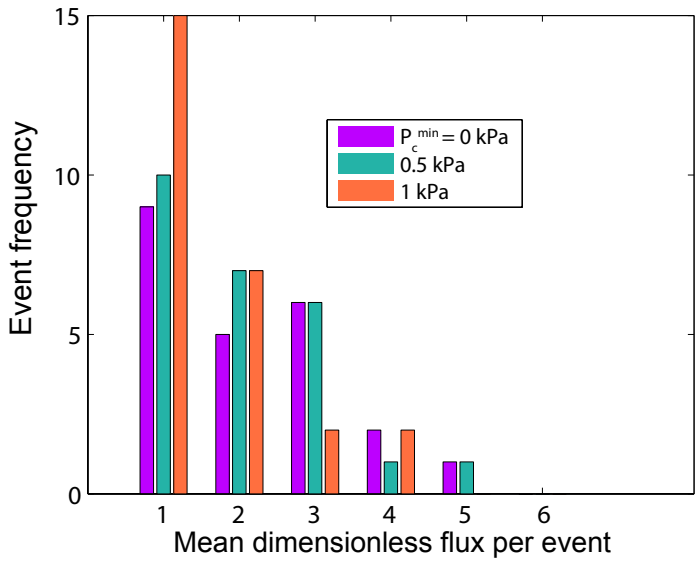

Figure 3-10: Histogram of mean flux rates per venting event for $P_c^{min} = 0, 0.5$, and 1 kPa. Larger minimum capillary pressure forces more frequent, smaller venting.

posite effect of encouraging frequent ebullition. During periods of rising hydrostatic pressure input, the gas pressure is held above the water pressure by P_c^{min}, and for larger values of this parameter the gas pressure is left higher at the end of plastic cavity compression. This high gas pressure encounters falling sediment stress during smaller drops in hydrostatic pressure, so the gas becomes mobile easier at every depth. Figure 3-9 shows that increasing P_c^{min} forces the cumulative release record to resemble better a straight line, composed of tiny variations rather than large jumps characteristic of vigorous venting periods. The transition to many, small releases may also be seen in the histogram in Figure 3-10.

3.4 Spatial resolution

Figure 3-11 shows that the model is insensitive to the vertical discretization, even at hourly resolution. This is important because the mobilization of gas in a particular control volume is a discrete process, and given a characteristic gas velocity α that is rapid relative to the rate at which the conduit extends in depth, the magnitude of individual bursts at high temporal resolution would be controlled by the rate at

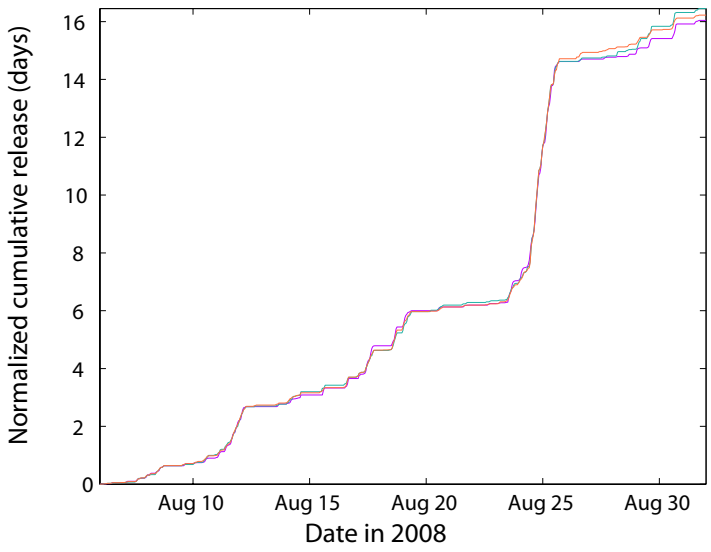

Figure 3-11: Confirmation that the flux rate is insensitive to the vertical resolution. The normalized cumulative release is the number of days required to exsolve the volume released and is almost indistinguishable for $nz = 16, 32$, and 64, even at hourly resolution.

which control volumes join the growing conduit. The models insensitivity to vertical resolution at hourly temporal resolution suggests that the value $\alpha = 2$ is small enough to avoid this numerical artifact. Because $t^* = 1$ day, $\alpha = 2$ corresponds to a bubble transit time of about 12 hours. Then during falling hydrostatic pressure and vertical extension of the conduit at an observed rate of about half a meter per day, multiple control volumes are mobilized within the time period of rise. In future work, the desire for greater temporal resolution may demand explicit modeling of more rapid bubble rise than considered here, and care must be taken to prevent the numerical scheme from impacting the temporal characteristics of ebullition.

Chapter 4

Results

4.1 Best fit

The results we seek are a good fit between the model-predicted and measured volumetric gas fluxes. Because the seasonally-integrated flux is tuned from the data and ratio of methane generated that is released, the overall magnitude of the model flux has little significance. The timing and *relative* magnitudes of the venting events, though, are characteristics that our model predicts given the input hydrostatic pressure variations and a limited number of unconstrained parameters. The four parameters tuned in the following results are the dimensionless gas flux rate through open conduits α, the model sediment depth h, minimum capillary pressure P_c^{min} and sediment cohesion C. An analysis of the model sensitivity to these parameters was performed in Chapter 3, and the best-fit results presented below will be interpreted in terms of their implications for the physical processes at play in lake sediments.

Figure 4-1 compares the modeled and measured daily-averaged gas fluxes at the lake surface, after tuning parameters to a local maximum correlation and minimum root mean squared error (RMSE) between data and model fluxes. This is not necessarily the global correlation maximum or RMSE minimum, as an exhaustive parameter search was not performed. However, the parameters fell within the expected range, and the fit is visually reasonable. Both records can be seen to respond with peaks in flux, or venting events, during periods of falling hydrostatic pressure. The model

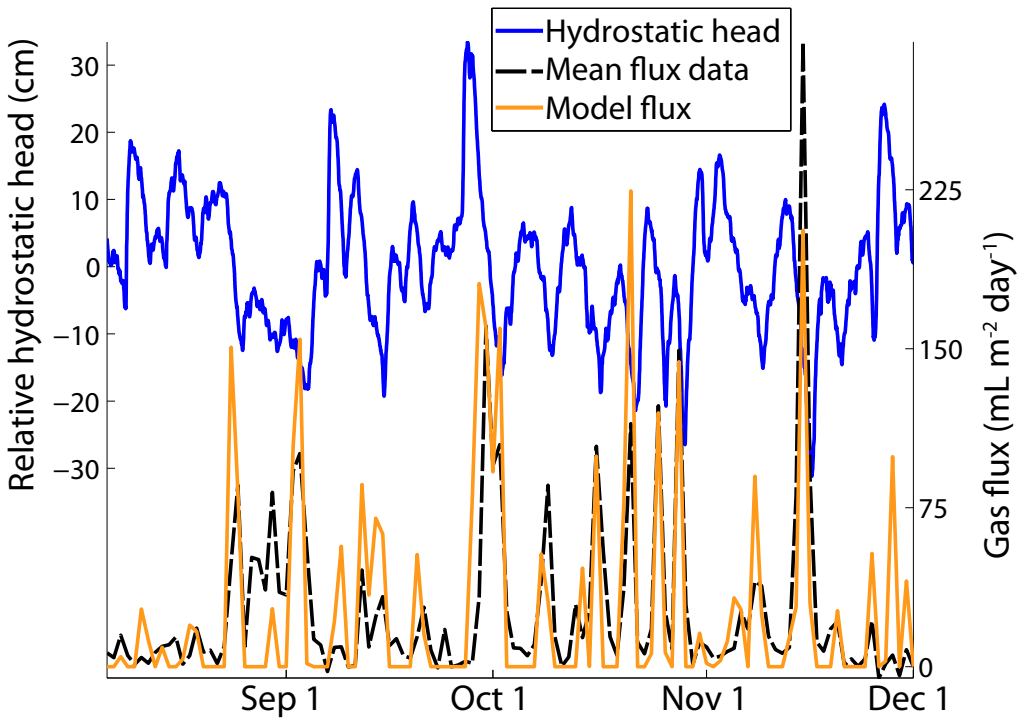

Figure 4-1: Best fit of data and model gas fluxes. The left axis and solid blue line show a time series of the hydrostatic pressure forcing, and the right axis shows the methane fluxes from the bubble trap data (black, dashed) and model (orange, solid). The fluxes are binned daily, and the cumulative model release is tuned to the data. The model accurately predicts the timing of large flux events and usually their magnitude, as well.

seems to capture the timing and relative magnitude of venting events. Spurious model flux peaks may correspond to venting events not recorded by any of the five traps because they were not placed over an active vent, while exaggerated peaks may correspond to slow-leakage events that mostly dissolved during the rise through the water column (a dynamic process neglected when $\bar{D}$ is assumed constant).

The parameter values that yielded this fit are $\alpha = 4$, $h = 1.5$ m, $P_c^{min} = 200$ Pa, and $C = 1000$ Pa. Increasing values of the gas loading efficiency γ_g above zero flattened the early flux peaks by keeping the conduits extent shallower, but then the late October peaks were excessively large compared with the data. The value of $\alpha = 4$ is high enough to reproduce the sharp flux peaks and evacuate gas from the sediment within about six hours of mobilizing it. Increasing α to 5 or reducing it to 3

decreases the correlation coefficient only slightly from 0.6 to 0.58 or 0.56, respectively, and increases the RMSE flux from 31 to 32 or 33.

A model sediment depth of 1.5 m allowed a balance of deep storage to provide high flux events during extreme pressure drops, and low total generation to allow small flux peaks otherwise. The correlation drops from 0.6 to 0.5 when h is increased to 2 m and to 0.4 when h is reduced to 1 m. The RMSE in flux increases to 40 mL m^{-2} day^{-1} in either case.

The minimum capillary pressure makes the model more prone to venting with small drops in hydrostatic head, and the best-fit value is $P_c^{min} = 200$ Pa. The daily flux results are not sensitive to values below this, but increasing even to 500 Pa increases the RMSE flux from 31 to 32 mL m^{-2} day^{-1} and reduces R^2 from 0.6 to 0.52. So, the minimum capillary pressure in the system does not seem to play a large role in controlling ebullition. The sediment cohesion has the opposite effect, of delaying or inhibiting gas releases, and $C = 1$ kPa gives the right amount of delay at the daily scale. Increasing C to 1.5 kPa reduces R^2 from 0.6 to 0.5 and increases the RMSE flux from 31 to 42 mL m^{-2} day^{-1}, while decreasing it to 0.5 kPa has the same effect on R^2 and increases RMSE flux to 33 mL m^{-2} day^{-1}. Sediment cohesion then appears to play a significant role in ebullition.

In all cases the sediments are assumed to be initially free of gas bubbles because an initial gas content elevates the August flux peaks even farther above the data without improving the overall fit. The value of $\bar{R}$ is measured after each model run and used in equation 2.57 to normalize the season-scale cumulative release. The parameter values tuned to match the model and data flux records in Figure 4-1 represent a local minimum of error and maximum of correlation in the five-dimensional space. While exhaustive parameter searching was not performed, the tuned values have reasonable physical implications, as will be discussed in Chapter 5.

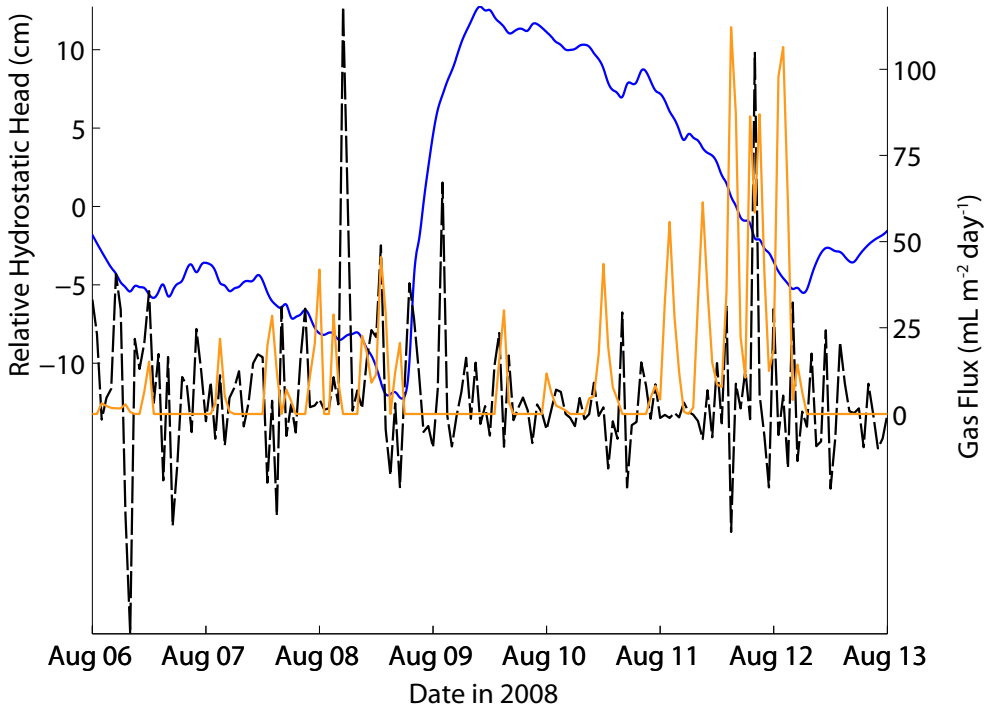

Figure 4-2: Time series of hydrostatic pressure forcing (left axis, blue color) and methane fluxes (right axis) from the bubble trap data (black, dashed) and model (orange, solid) with hourly binning. The negative data fluxes are artifacts of surface waves acting on the pressure sensor used to estimate gas volume in the bubble traps, which were suspended by buoys below the surface. Such artifacts erode confidence in physical inferences based on fitting a model to the data at this time scale.

4.2 Increased temporal resolution

The ultimate goal of this modeling effort is to estimate the lake-wide atmospheric methane release in a way that can be applied to other lakes. One component of such an application is understanding the methane loss from bubbles during their rise through the water column, which as discussed in Chapter 1 may depend strongly on the rate and mechanism of release. In particular, dissolution depends on the concentration of bubbles in a rising plume, and estimating the population of bubbles rising at about 25 cm sec^{-1} requires temporal resolution on the order of seconds to minutes, not hours or days. We may find through field work that such effects do not play a role because the fluxes at the sediment surface are simply too small to generate any bubble interaction, but for now the unconstrained areal spread mechanism and possibility that the few deployed traps missed the most vigorous venting sites prevent us from ruling them out. If we must consider the temporal concentration of venting on the minute timescale, more sophisticated modeling and more reliable data will be required. Figure 4-2 shows how the data, even averaged over five traps and smoothed with a one-hour moving-average filter, still display negative gas flux rates.

4.3 Multiple Traps

The data in Figure 4-1 are the average of the five traps with continuous flux records over the fall of 2008. The flux records from *individual* traps in Figure 1-3 show some synchronicity but also more intense flux rates during less-frequent events. This emphasis on low-frequency and high-power venting is visible both in a histogram (Figure 4-3) and in a comparison of the power spectra of the model against the average data and those from individual traps (Figure 4-4), which have much more power concentrated at monthly frequencies than either the average data or the model.

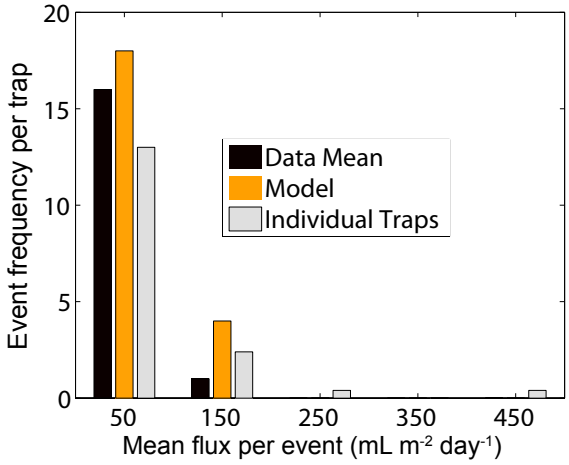

Figure 4-3: Histogram of mean gas flux rate per event for the mean data, individual trap data, and model output. A flux event is defined as a continuous daily flux rate above 15 mL m^{-2} day^{-1}. Because the sum of histograms from five individual traps records more flux events than an individual record (model or mean data), the "individual trap" histogram is normalized by the number of traps. Consistent with Figure 4-1, the data mean and model distributions match, but both are missing events with large flux rates seen in the record from individual traps ("9mA" in particular saw more vigorous venting – see green line in Figure 1-3).

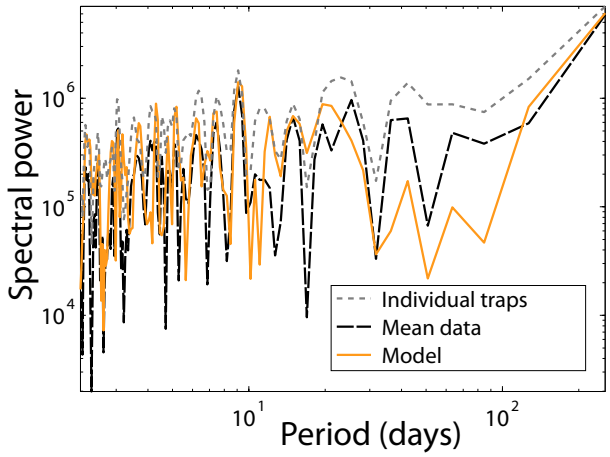

Figure 4-4: Power spectra for individual traps, mean data from five traps, and model output. In the 30-100 day range the mean data, and even more so the model flux, lack the spectral power of the flux record from individual traps. This suggests that individual traps have some delay mechanism that imposes a month-scale induction time averaged out by the mean data and not captured by the model.

Chapter 5

Discussion and Conclusions

5.1 Implications of data-model fit

The goal of this modeling work was to identify the dominant mechanism linking methane ebullition in lakes to changes in water level and atmospheric pressure. we hypothesized that the combination of plastic gas cavity expansion in deformable sediments and multiphase flow through vertical conduits was sufficient to explain this link. The mechanistic, numerical model developed was forced with a record of hydrostatic pressure at Upper Mystic Lake, MA, and the predicted methane fluxes were tuned against recorded methane fluxes at the surface. Because the initial correlation between the hydrostatic forcing and ebullition was so poor ($R^2 = 0.08$), the model had to capture significant nonlinear behavior. We may conclude, from the visual match and greatly-improved correlation between the predicted and measured fluxes ($R^2 = 0.6$) compared with the hydrostatic forcing, that the proposed model is valid for predicting the temporal concentration of ebullition at the daily timescale given that forcing. The combined poromechanics and multiphase flow equations may be said to represent the physics at play because the tuned parameter values have reasonable physical interpretations, as discussed below.

The model depth of $h = 1.5$ m suggests that free-gas transport within the sediment occurs primarily within this depth range. This is consistent with our knowledge that the methane is of totally biological origin, that no deep, geothermal sources contribute

to the release. The assumption that the gas exsolves uniformly with depth may be refined with further field investigation. If, for example, methanogenesis peaks at a shallow depth and decreases exponentially downward, then the active depth range would be shallower, and a better fit would be obtained by assuming less-permeable flow conduits.

The tuned sediment cohesion $C = 1$ kPa has a clear physical relationship to plastic cavity expansion and should strongly impact the ebullition record. The analysis in Chapter 4 shows that the data-model fit is sensitive to C in this range. This tuned cohesion value is small compared with those found by Johnson *et al.* (2002), which showed pressure fluctuations of up to 5 kPa during cycles of pressurization and fracturing by individual bubbles [27]. This supports the interpretation that lake sediments are poorly cohesive and suggests that neglecting transient bubble pressurization by exsolution is a valid approximation for this system. Future laboratory experiments should be able to constrain further this parameter.

The best-fit minimum capillary pressure of 200 Pa suggests that gas bubbles of sufficient size to impact the ebullition record may be 1 mm in diameter. Such bubbles are larger than the void spaces measured in synthetic gassy sediments [55], and the mismatch may be explained in at least two ways. Either the lower-stress conditions in lake sediments allow larger gas cavities, or plastic cavity compression is not related to capillary effects and equation 2.19 is not appropriate. Even so, the data-model fit suggests that plastic cavity expansion and compression is a valid mechanism for evolving the gas pressure in lake sediments. Fruitful model improvements may come from investigating dynamic plastic deformation limits. For example, equation 2.15 suggests that the scaling $C \sim S_g^{-\frac{1}{3}}$ could capture the increase in gas effective stress with cavity compression (reduction in S_g) based on the dynamics of a perfectly plastic sediment-water matrix [61].

The open-conduit dimensionless conductivity value $\alpha = 4$ implies that a bubble rises through the sediment column in about 6 hours once it is mobilized. This value corresponds to a permeability of 10^{-13} m^2, which is small relative to the expected effective permeability of a 100-μm conduit [50]. However, a lower permeability is

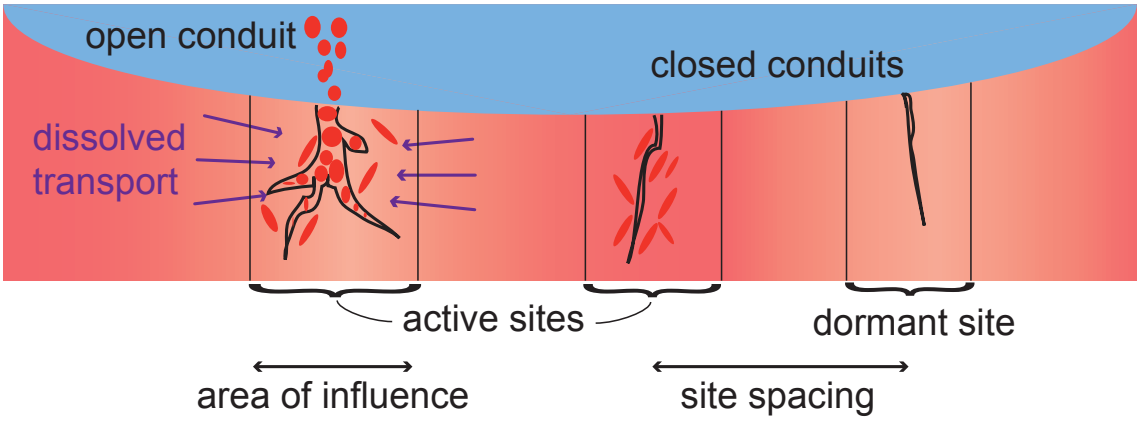

Figure 5-1: Schematic relationship between three possible venting site states. The far left venting site contains multiple exsolved bubbles that have currently activated their ebullition mechanism and are escaping into the water column. The local pressure drop within the site drives not only further exsolution from the methane-rich pore water, but also some lateral pore water advection. This dissolved methane transport may help maintain the methane concentrations within the area of influence of the free-gas flow mechanisms by pulling in methane from outside that area. The timescales of vertical and horizontal transport should determine the characteristic size and persistence of active venting sites. Even as bubbles in the left site escape, those at the central site remain trapped, perhaps because the bubble growth pattern inhibits opening of flow conduits during some induction time after a venting event.

reasonable for our model because a single conduit drains a characteristic area, possibly on the scale of meters, and the conduit permeability should account for both vertical transport and lateral transfer of gas within the venting site to the conduit. So, the low permeability is consistent with the horizontal homogenization into a one-dimensional model.

The model was shown to match the flux history and distribution from the mean of five bubble trap records, but Section 4.3 demonstrates that the same was not true of individual traps. Individual traps typically record more vigorous and less frequent ebullition events than their average because not all venting sites activate simultaneously (Figure 1-3). If individual traps reflect the behavior of individual venting sites better than the average, then this observation implies some mechanism is forcing an induction time between releases from individual sites. For example, the pressure gradients away from venting sites created after gas release may drive slow lateral methane transport. Figure 5-1 highlights some proposed behaviors, including lateral methane transport and dormancy of vents. The current model represents better the upscaled, lake-wide gas flux signal character than that from any one location. In the sense that we seek to model the lake-wide atmospheric flux, this is fortunate. However, because we hypothesize that the bubble interactions that attenuate the methane release depend on the spatial and temporal concentration of flux events, this observation motivates us to capture whatever mechanism causes the induction time associated with events from individual venting sites. Future work should incorporate the behavior of individual sites and characterize their interactions and relationship in space and time.

The seasonal cumulative methane flux from the model is either estimated from the data, or even tuned to match the data and model gas fluxes (see Section 2.5.1). So, the temporal concentration of flux into peaks of relative height, width and timing is the unconstrained contribution of the numerical model. This tuning was performed by assuming that neither the fraction methane in bubbles rising through the water column that dissolves, nor the spacing of venting sites, depended on the rate of gas release from the sediments. Because a reasonable fit was obtained with this

assumption, we could conclude that bubble dissolution is insensitive to the rate of release. However, research on the bubble interactions in plumes [38, 37, 19] and the relationship between bubble sizes and rates of release [22, 64] motivates us to refine the model further by considering these dynamic dissolution effects. By linking the mode of gas release to dissolution, these effects determine how strongly the lake system attenuates atmospheric methane emissions from the amount generated in lake sediments. If the lake's effective "chemical resistance" to the greenhouse potential of methane, via dissolution and oxidation of CH_4 to CO_2, depends on ebullition parameters that may be measured, then the global atmospheric methane contribution from lakes may be better constrained.

5.2 Future Work

In addition to adding complexity to the model, we will seek to observe directly the dynamic flow conduit mechanism proposed and constrain the physical parameters with field observations. Figure 5-2 diagrams a number of proposed field measurements and describes how each may help constrain the dynamics of methane venting from lake sediments. For example, video analysis of rising bubble plumes (label (h)) will allow us to quantify accurately the density and size distribution of bubbles, both of which impact the fraction dissolved during rise (Figure 1-6). Sediment-surface bubble traps (5-2 (f)) will capture the gas flux from identified venting sites and will be impacted less by dissolution and surface-wave corruption, which hinder data analysis and model development at better than daily resolution. Repeated seismic surveys (5-2 (d)) will constrain the longevity of venting sites and determine whether dormant sites (Figure 5-1) preferentially re-activate because preexisting conduits heal with lower sediment cohesion. Push cores of the shallow sediments (5-2 (c)) will allow estimates of the evolving gas content and determine the validity of the undrained assumption via flow permeability tests. Not shown on this figure is another possible field observation, the 2D imaging of trapped bubbles and flow conduits using an X-ray source and film inserted directly into a known venting site. If a bubble trap

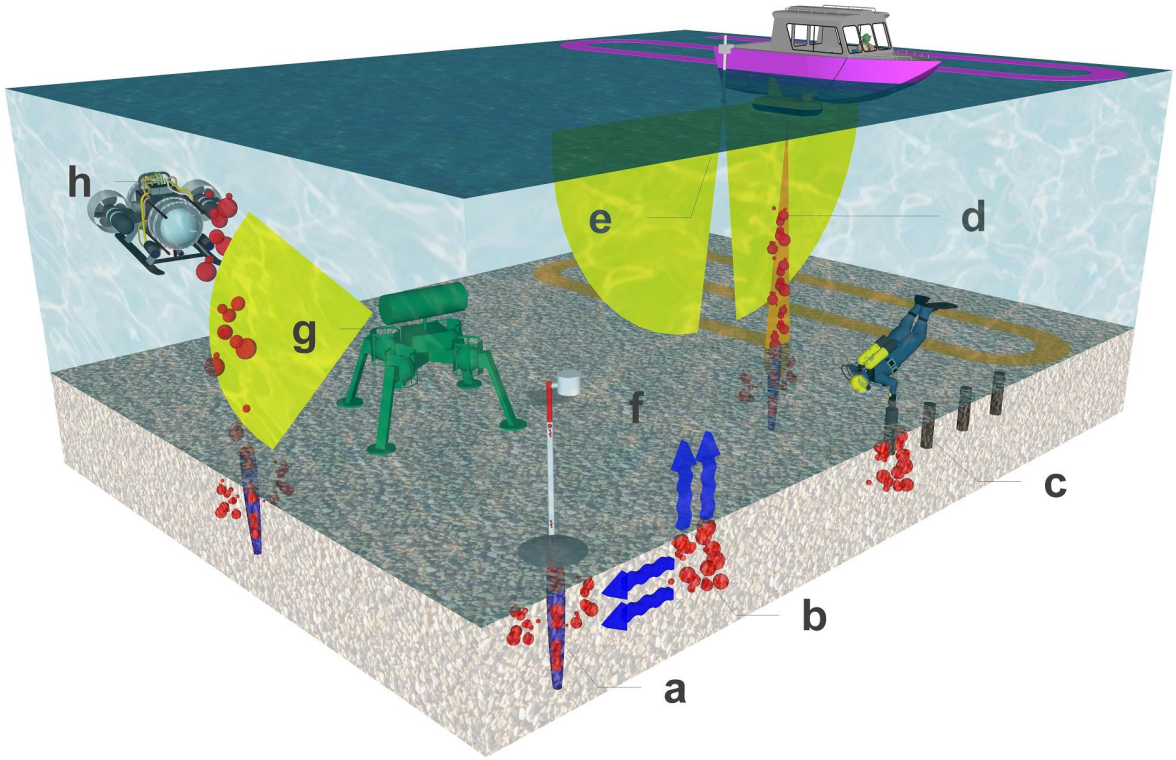

Figure 5-2: Cartoon placing the central processes and field techniques into a region of lake overlying methane-generating sediments: (a) Methane generated in the sediments forms bubbles (red, enlarged) that are released through open vertical flow conduits (purple); (b) Methane is transported as a solute (wavy blue lines) laterally toward venting sites within the sediments and vertically into the water column; (c) Transect of push cores characterizes sediment properties; (d) Boat-based seismic survey, with orange downward-facing chirp signal penetrating the sediments, detects trapped gas. Orange switchback pattern projected on sediment surface depicts boat path and survey coverage; (e) Sidescan sonar survey (yellow fan-shaped ping) detects a bubble plume (red) in the water column rising from venting sites; (f) Bubble trap records the free-gas flux at the sediment surface with high resolution; (g) Ping from an acoustic transducer rotating on a benthic platform captures the spatiotemporal variability of gas releases; (h) Video recording of rising plumes by ROV captures bubble size distribution and plume effects. Multiple sub-models downloaded from the Google 3D Warehouse

is positioned just above this site, then it could trigger the X-ray source exposure triggered when bubble release is detected.

While the current model is almost completely insensitive to the mean water depth parameter, which impacts the absolute pressures but not relative changes, Figure 1-6 shows that incorporating a depth-dependent dissolution model will make the depth more important. An improved bathymetric map, already under development thanks to initial field work by the USGS's Carolyn Ruppel on UML, will allow us to incorporate the distribution of depths if not explicitly model the distributed lake system to improve the atmospheric release estimate. The primary unknown not scheduled to be addressed is the fate of dissolved methane in the deep, anoxic hypolimnion, which may escape to the atmosphere or be oxidized first to carbon dioxide.

The proposed field campaign will be supplemented by laboratory experiments. Small sediment microcosms may be imaged in two dimensions (ant farm-shaped containment cell) with a high-speed camera and in three dimensions (aquarium-shaped) with a medical X-ray computer-aided tomography system. Gas may be fed into the system either by a needle [4], from a free-gas reservoir below, by exsolution from source pore water supersaturated by methane, or even by incubation of anoxic methanogenic communities. As the gas bubbles grow and mobilize with controlled variations in the overlying water level, we may observe both the morphology and rate of gas release. Simultaneous observation of bubbles in the sediment and water column will support or disprove the proposed link between the rate of gas release and free bubble size. The combination of these laboratory and field investigations will support refinements of the model both to describe the mechanisms governing gas release and to constrain the quantity of methane that lakes contribute to the atmosphere.

Bibliography

[1] M. Biot. General theory of three-dimensional consolidation. *Journal of Applied Physics*, 12(2):155–164, 1941.

[2] A. W. Bishop. The principle of effective stress. *Teknisk Ukeblad*, 39:859863, 1959.

[3] J. Boles, J. Clark, I. Leifer, and L. Washburn. Temporal variation in natural methane seep rate due to tides, coal oil point area, california. *Journal of Geophysical Research-Oceans*, 106(C11):27077–27086, 2001.

[4] B. Boudreau, C. Algar, B. Johnson, I. Croudace, A. Reed, Y. Furukawa, K. Dorgan, P. Jumars, A. Grader, and B. Gardiner. Bubble growth and rise in soft sediments. *Geology*, 33(6):517–520, 2005.

[5] R. J. S. Brown and J. Korringa. On the dependence of elastic properties of a proous rock on compressibility of pore fluid. *Geophysics*, 40(4):608–616, 1975.

[6] J. Chanton, C. Martens, and C. Kelley. Gas transport from methane-saturated, tidal freshwater and wetland sediments. *Limnology and Oceanography*, 34(5)(5):807–819, 1989.

[7] Y.-H. Chen and R. G. Prinn. Atmospheric modeling of high- and low-frequency methane observations: Importance of interannually varying transport. *Journal of Geophysical Research-Atmospheres*, 110(D10), 2005.

[8] Y.-H. Chen and R. G. Prinn. Estimation of atmospheric methane emissions between 1996 and 2001 using a three-dimensional global chemical transport model. *Journal of Geophysical Research-Atmospheres*, 111(D10), 2006.

[9] O. Coussy. *Poromechanics*. Wiley (West Sussex, England), 2004.

[10] P. Crill, K. Bartlett, J. Wilson, D. Sebacher, R. Harriss, J. Melack, S. Macintyre, L. Lesack, and L. Smithmorrill. Tropospheric methane from an amazonian floodplane lake. *Journal of Geophysical Research-Atmospheres*, 93(D2):1564–1570, 1988.

[11] T. Delsontro, D. F. McGinnis, S. Sobek, I. Ostrovsky, and B. Wehrli. Extreme methane emissions from a swiss hydropower reservoir: Contribution from bubbling sediments. *Environmental Science and Technology*, 44(7):2419–2425, 2010.

[12] K. L. Denman, G. Brasseur, A. Chidthaisong, P. Ciais, P. M. Cox, R. E. Dickinson, D. Hauglustaine, C. Heinze, E. Holland, D. Jacob, U. Lohmann, S. Ramachandran, P. L. da Silva Dias, S. C. Wofsy, and X. Zhang. Couplings between changes in the climate system and biogeochemistry. In S. Solomon, D. Qin, M. Manning, Z. Chen, M. Marquis, K. Averyt, M.Tignor, and H. Miller, editors, *Climate Change 2007: The Physical Science Basis. Contribution of Working Group I to the Fourth Assessment Report of the Intergovernmental Panel on Climate Change*, pages 499–588. Cambridge University Press, Cambridge, United Kingdom and New York, NY, USA, 2007.

[13] A. Dove, N. Roulet, P. Crill, J. Chanton, and R. Bourbonniere. Methane dynamics of a northern boreal beaver pond. *Ecoscience*, 6(4):577–586, 1999.

[14] Z. Duan and S. Mao. A thermodynamic model for calculating methane solubility, density and gas phase composition of methane-bearing aqueous fluids from 273 to 523 k and from 1 to 2000 bar. *Geochimica et Cosmochimica Acta*, 70(13):3369–3386, 2006.

[15] D. H. Ehhalt. The atmospheric cycle of methane. *Tellus*, 26(1-2):58–70, 1974.

[16] E. Fechner-Levy and H. Hemond. Trapped methane volume and potential effects on methane ebullition in a northern peatland. *Limnology and Oceanography*, 41(7):1375–1383, 1996.

[17] P. Flemings, X. Liu, and W. Winters. Critical pressure and multiphase flow in blake ridge gas hydrates. *Geology*, 31(12):1057–1060, 2003.

[18] F. Gassmann. ber die elastizitt poroser medien. *Vierteljahrsschrift der Naturforschenden Gesellschaft in Zrich*, 96:1–23, 1951.

[19] X. Gong, S. Takagi, and Y. Matsumoto. The effect of bubble-induced liquid flow on mass transfer in bubble plumes. *International Journal of Multiphase Flow*, 35(2):155–162, 2009.

[20] W. G. Gray and B. A. Schrefler. Analysis of the solid phase stress tensor in multiphase porous media. *International Journal for Numerical and Analytical Methods in Geomechanics*, 31(4):541–581, 2007.

[21] J. Greinert and D. F. McGinnis. Single bubble dissolution model - the graphical user interface sibu-gui. *Environmental Modelling & Software*, 24(8):1012–1013, 2009.

[22] J. Greinert and B. Nutzel. Hydroacoustic experiments to establish a method for the determination of methane bubble fluxes at cold seeps. *Geo-Marine Letters*, 24(2):75–85, 2004.

[23] M. Haeckel, B. P. Boudreau, and K. Wallmann. Bubble-induced porewater mixing: A 3-d model for deep porewater irrigation. *Geochimica et Cosmochimica Acta*, 71(21):5135–5154, 2007.

[24] W. K. Hamblin and E. H. Christiansen. *Earth's Dynamic Systems*. Pearson Education, Inc., New Jersey, 2004.

[25] T. Hoehler, M. Alperin, D. Albert, and C. Martens. Field and laboratory studies of methane oxidation in an anoxic marine sediment - evidence for a methanogen-sulfate reducer consortium. *Global Biogeochemical Cycles*, 8(4):451–463, 1994.

[26] A. K. Jain and R. Juanes. Preferential mode of gas invasion in sediments: Grain-scale mechanistic model of coupled multiphase fluid flow and sediment mechanics. *Journal of Geophysical Research-Solid Earth*, 114, 2009.

[27] B. Johnson, B. Boudreau, B. Gardiner, and R. Maass. Mechanical response of sediments to bubble growth. *Marine Geology*, 187(3-4):347–363, 2002.

[28] J. Joyce and P. W. Jewell. Physical controls on methane ebullition from reservoirs and lakes. *Environmental & Engineering Geoscience*, IX(2):167–178, 2003.

[29] J. Kalff. *Limnology*. Prentice Hall, New Jersey, 2002.

[30] G. v. d. Kamp and J. E. Gale. Theory of earth tide and barometric effects in porous formations with compressible grains. *Water Resources Research*, 19(2):538–544, 1983.

[31] M. Keller and R. Stallard. Methane emission by bubbling from gatun lake, panama. *Journal of Geophysical Research-Atmospheres*, 99(D4):8307–8319, 1994.

[32] C. Kelly and D. Chynoweth. The contributiions of temperature and of the input of organic matter in controlling rates of sediment methanogenesis. *Limnology and Oceanography*, 26(5):891–897, 1981.

[33] S. Klein. Sediment porewater exchange and solute release during ebullition. *Marine Chemistry*, 102(1-2, Sp. Iss. SI):60–71, 2006.

[34] P. K. Kundu and I. M. Cohen. *Fluid Mechanics*. Elsevier Academic Press, 2004.

[35] J. Lay, T. Miyahara, and T. Noike. Methane release rate and methanogenic bacterial populations in lake sediments. *Water Research*, 30(4):901–908, 1996.

[36] I. Leifer and J. Boles. Turbine tent measurements of marine hydrocarbon seeps on subhourly timescales. *Journal of Geophysical Research-Oceans*, 110(C1), 2005.

[37] I. Leifer, B. P. Luyendyk, J. Boles, and J. F. Clark. Natural marine seepage blowout: Contribution to atmospheric methane. *Global Biogeochemical Cycles*, 20(3), 2006.

[38] A. Leitch and W. Baines. Liquid volume flux in a weak bubble plume. *Journal of Fluid Mechanics*, 205:77–98, 1989.

[39] A. Liikanen, T. Murtoniemi, H. Tanskanen, T. Vaisanen, and P. Martikainen. Effects of temperature and oxygen availability on greenhouse gas and nutrient dynamics in sediment of a eutrophic mid-boreal lake. *Biogeochemistry*, 59(3):269–286, 2002.

[40] X. Liu and P. Flemings. Dynamic response of oceanic hydrates to sea level drop. *Geophysical Research Letters*, 36, 2009.

[41] X. Liu and P. B. Flemings. Dynamic multiphase flow model of hydrate formation in marine sediments. *Journal of Geophysical Research-Solid Earth*, 112(B3), 2007.

[42] C. Martens, D. Albert, and M. Alperin. Stable isotope tracing of anaerobic methane oxidation in the gassy sediments of eckernforde bay, german baltic sea. *American Journal of Science*, 299(7-9):589–610, 1999.

[43] C. Martens and J. val Klump. Biogeochemical cycling in an organic-rich coastal marine basin. 1. methane sediment-water exchange processes. *Geochimica et Cosmochimica Acta*, 44(3):471–490, 1980.

[44] M. D. Mattson and G. Likens. Air pressure and methane fluxes. *Nature*, 347:718–719, 1990.

[45] D. F. McGinnis, J. Greinert, Y. Artemov, S. E. Beaubien, and A. Wuest. Fate of rising methane bubbles in stratified waters: How much methane reaches the atmosphere? *Journal of Geophysical Research-Oceans*, 111(C9), 2006.

[46] J. M. Mogollon, I. L'Heureux, A. W. Dale, and P. Regnier. Methane gas-phase dynamics in marine sediments: a model study. *American Journal of Science*, 309(3):189–220, 2009.

[47] M. Muskat. *Physical Principles of Oil Production*. McGraw-Hill Book Co. (New York), 1949.

[48] S. Nageswaran. *Effect of gas bubbles on the sea bed behaviour*. PhD thesis, Univerisity of Oxford, 1983.

[49] T. Nakamura, Y. Nojiri, M. Utsumi, T. Nozawa, and A. Otsuki. Methane emission to the atmosphere and cycling in a shallow eutrophic lake. *Archiv fur Hydrobiologie*, 144(4):383–407, 1999.

[50] J. Nimblett and C. Ruppel. Permeability evolution during the formation of gas hydrates in marine sediments. *Journal of Geophysical Research-Solid Earth*, 108(B9), 2003.

[51] S. J. Poulos. *Advance Dam Engineering for Design*, chapter Liquefaction Related Phenomena, pages 292–320. Van Nostrand Reinhold, 1989.

[52] J. W. M. Rudd and R. D. Hamilton. Methane cycling in a eutrophic shield lake and its effects on whole lake metabolism. *Limnology and Oceanography*, 23(2):337–348, 1978.

[53] A. H. Sawyer, P. Flemings, D. Elsworth, and M. Kinoshita. Response of submarine hydrologic monitoring instruments to formation pressure changes: Theory and application to nankai advanced corks. *Journal of Geophysical Research-Solid Earth*, 113(B1), 2008.

[54] K. A. G. Schmidt, G. K. Folas, and B. Kvamme. Calculation of the interfacial tension of the methane-water system with the linear gradient theory. *Fluid Phase Equilibria*, 261(1-2, Sp. Iss. SI):230–237, 2007.

[55] G. C. Sills, S. J. Wheeler, S. D. Thomas, and N. T. Gardner. Behavior of offshore soils containing gas-bubbles. *Geotechnique*, 41(2):227–241, 1991.

[56] A. Skempton. *Pore Pressure and Suction in Soils*, chapter Effective Stress in Soils, Concrete and Rocks, pages 4–16. Butterworths, London, 1960.

[57] S. Solomon, D. Qin, M. Manning, Z. Chen, M. Marquis, K. Averyt, M.Tignor, and H. Miller, editors. *Climate Change 2007: The Physical Science Basis. Contribution of Working Group I to the Fourth Assessment Report of the Intergovernmental Panel on Climate Change*. Cambridge Univ. Press, New York, 2007.

[58] A. D. W. Sparks. Theoretical consideration of stress equations for partly saturated soils. In *3rd African Conf: Soil Mech. Fd Enang. Salisbury. Rhodesia*, volume 1, pages 215–218, 1963.

[59] R. Strayer and J. Tiedje. In situ methane production in a small, hypereutrophic, hard-water lake: loss of methane from sediments by vertical diffusion and ebullition. *Limnology and Oceanography*, 23(6):1201–1206, 1978.

[60] K. Terzaghi. *Erdbaumechanik*. Franz Deuticke, Vienna, 1925.

[61] S. D. Thomas. *The consolidation behaviour of gassy soil*. PhD thesis, University of Oxford, 1987.

[62] T. Tokida, T. Miyazaki, M. Mizoguchi, O. Nagata, F. Takakai, A. Kagemoto, and R. Hatano. Falling atmospheric pressure as a trigger for methane ebullition from peatland. *Global Biogeochemical Cycles*, 21(2), 2007.

[63] M. Torres, J. McManus, D. Hammond, M. de Angelis, K. Heeschen, S. Colbert, M. Tryon, K. Brown, and E. Suess. Fluid and chemical fluxes in and out of sediments hosting methane hydrate deposits on hydrate ridge, or, i: Hydrological provinces. *Earth and Planetary Science Letters*, 201(3-4):525 – 540, 2002.

[64] G. Vallebuona, A. Casali, and W. Kracht. Characterization and modeling of bubbles size distribution in mechanical flotation cells. *Revista de Metalurgia*, 41(4):243–250, 2005.

[65] B. van Leer. Towards the ultimate conservative difference scheme iii. upstream-centered finite-difference schemes for ideal compressible flow. *Journal of Computational Physics*, 23:263–75, 1977.

[66] C. Varadharajan. *Magnitude and Spatio-Temporal Variability of Methane Emissions from a Eutrophic Freshwater Lake*. PhD thesis, Massachusetts Institute of Technology, 2009.

[67] C. Varadharajan, R. Hermosillo, and H. F. Hemond. A low-cost automated trap to measure bubbling gas fluxes. *Limnological and Oceanographical Methods*, In Press.

[68] K. M. Walter, S. A. Zimov, J. P. Chanton, D. Verbyla, and F. S. Chapin, III. Methane bubbling from siberian thaw lakes as a positive feedback to climate warming. *Nature*, 443(7107):71–75, 2006.

[69] H. F. Wang. *Theory of Linear Poroelasticity with Applications to Geomechanics and HydroGeology*. Princeton University Press, 2000.

[70] K. Wang and E. Davis. Theory for the propagation of tidally induced pore pressure variations in layered subseafloor formations. *Journal of Geophysical Research-Solid Earth*, 101(B5):11483–11495, 1996.

[71] K. Wang, E. Davis, and G. van der Kamp. Theory for the effects of free gas in subsea formations on tidal pore pressure variations and seafloor displacements. *Journal of Geophysical Research-Solid Earth*, 103(B6):12339–12353, 1998.

[72] S. Wheeler. *The stress-strain behaviour of soils containing gas bubbles*. PhD thesis, University of Oxford, 1986.

[73] S. Wheeler. A conceptual-model for soils containing large gas-bubbles. *Geotechnique*, 38(3):389–397, 1988.

[74] S. Wheeler and T. Gardner. Elastic-moduli of soils containing large gas-bubbles. *Geotechnique*, 39(2):333–342, 1989.

[75] S. J. Wheeler. Movement of large gas-bubbles in unsaturated fine-grained sediments. *Marine Geotechnology*, 9(2):113–129, 1990.

[76] S. J. Wheeler, W. K. Sham, and S. D. Thomas. Gas-pressure in unsaturated offshore soils. *Canadian Geotechnical Journal*, 27(1):79–89, 1990.

[77] A. Yamamoto, M. Hirota, S. Suzuki, Y. Oe, P. Zhang, and S. Mariko. Effects of tidal fluctuations on co2 and ch4 fluxes in the littoral zone of a brackish-water lake. *Limnology*, 10(3):228–237, 2009.

[78] S. H. Zinder. *Methanogenesis: Ecology, Physiology, Biochemistry and Genetics*, chapter Physiological ecology of methanogens. Chapman and Hall, 1993.